

Observing Upper Ocean Stratification during Strong Diurnal SST Variation Events in the Suppressed Phase of the MJO

Je-Yuan Hsu¹, Ming Feng², and Susan Wijffels³

¹National Taiwan University

²CSIRO Oceans and Atmosphere

³Woods Hole Oceanographic Institution, Physical Oceanography

November 24, 2022

Abstract

Six ALAMO floats are deployed within the tropical warm pool of the eastern Indian Ocean, to study the thermal stratification in the diurnal warm layer (DWL) during strong diurnal SST variation (DV SST) prior to the onset of Madden-Julian Oscillations (MJO). Strong DV SST of > 2 °C is measured by four floats before the passage of a MJO event (i.e., during the suppressed phase), when the peak insolation > 1000 W m⁻² and the wind speed < 3 m s⁻¹. Even after the occurrence of daytime peak SST, the temperature gradient in the DWL can still extend to > 10 m until the midnight, which may be driven by the turbulent mixing at the base of DWL. Interestingly, the foundation SST (SST_{fd}) at three floats increases rapidly from 26.4 °C to > 27.6 °C over two days, coincident with the shoaling of surface mixed layer depth (MLD) by more than 20 m. The strongly stratified near surface layer may sustain higher SSTs and enhance air-sea heat fluxes until the onset of stronger winds. The KPP mixing scheme used in a 1-D model can simulate the observed DV SST magnitude reliably, but fail to predict the rapid increase of SST_{fd}. The magnitude of DV SST is affected by the near surface stratification, but the SST_{fd} is modulated by the evolution of stratification above the MLD. Future field measurements in the upper ocean during diurnal warming are proposed to help improve air-sea flux simulations and the forecast of MJOs.

Hosted file

supplemental_v1.docx available at <https://authorea.com/users/547412/articles/602735-observing-upper-ocean-stratification-during-strong-diurnal-sst-variation-events-in-the-suppressed-phase-of-the-mjo>

22 **Abstract**

23 Six ALAMO floats are deployed within the tropical warm pool of the eastern Indian Ocean, to
24 study the thermal stratification in the diurnal warm layer (DWL) during strong diurnal SST
25 variation (DV SST) prior to the onset of Madden-Julian Oscillations (MJO). Strong DV SST of >
26 2 °C is measured by four floats before the passage of a MJO event (i.e., during the suppressed
27 phase), when the peak insolation > 1000 W m⁻² and the wind speed < 3 m s⁻¹. Even after the
28 occurrence of daytime peak SST, the temperature gradient in the DWL can still extend to > 10 m
29 until the midnight, which may be driven by the turbulent mixing at the base of DWL.
30 Interestingly, the foundation SST (SST_{fnd}) at three floats increases rapidly from 26.4 °C to > 27.6
31 °C over two days, coincident with the shoaling of surface mixed layer depth (MLD) by more
32 than 20 m. The strongly stratified near surface layer may sustain higher SSTs and enhance air-
33 sea heat fluxes until the onset of stronger winds. The KPP mixing scheme used in a 1-D model
34 can simulate the observed DV SST magnitude reliably, but fail to predict the rapid increase of
35 SST_{fnd} . The magnitude of DV SST is affected by the near surface stratification, but the SST_{fnd} is
36 modulated by the evolution of stratification above the MLD. Future field measurements in the
37 upper ocean during diurnal warming are proposed to help improve air-sea flux simulations and
38 the forecast of MJOs.

39

40 **1. Introduction**

41 Air-sea heat fluxes over high sea surface temperatures (SST) of the tropical warm pools
42 (TWPs) have a critical influence on the atmospheric general circulation. These TWPs frequently
43 feature low wind conditions and thus experience ubiquitous and strong diurnal variations of SST
44 (DV SST). Latent and sensible heat fluxes, modulated by the SST, can affect the onset and
45 timing of intra-seasonal weather systems such as the MJOs (Zhang 2005; Maloney 2009; Seo et
46 al. 2014; Sobel et al. 2014). While the intrinsic time scale of MJOs is longer than a week, the
47 coupled model forecasts of MJOs can be influenced significantly by DV SSTs through impacts
48 on daily-mean SST (Bernie et al. 2008; Rupert and Johnson 2015; Demott et al. 2015). Modeling
49 the diurnal variations of the upper ocean remains challenging (Kawai and Wada 2007). To
50 forecast the DV SST accurately, turbulent mixing in the upper ocean must also be simulated
51 accurately, which involves the forecast on both the shear and density stratification for inducing
52 shear instability mixing. Therefore, exploring the diurnal SST variations and associated
53 evolution of stratified layers near the ocean surface may be crucial for improving the MJO
54 forecast.

55 The evolution of stratified layers (Fig. 1) above the seasonal thermocline during the DV
56 SST has been discussed in several previous studies such as Brainerd and Gregg (1993a) and
57 Sutherland et al. (2016). Under low wind conditions, the absorption of insolation during the
58 daytime forms a sharp vertical temperature gradient in the surface mixed layer, termed the
59 diurnal thermocline (Kudryavtsev and Soloviev 1990; Caldwell et al. 1997). The diurnal warm
60 layer (DWL, Sui et al. 1997; Matthews et al. 2014; Sutherland et al. 2016; Moulin et al. 2018;
61 Hughes et al. 2020), spanning the ocean surface to the base of diurnal thermocline, can modify
62 the magnitude of DV SST through the inhibition of turbulent mixing across its base (Fairall et al.

63 1996b; Bellenger and Duvel 2009; Moulin et al. 2018). Below, the layer between the DWL and
64 the top of the seasonal thermocline is termed the remnant layer (RL, Brainerd and Gregg 1993a;
65 Caldwell et al. 1997), which can be regarded as a fossil mixed layer formed during the previous
66 night due to convective cooling. The penetrative solar radiation can not only form the DWL, but
67 also restratify the RL (Brainerd and Gregg 1993a). After a late afternoon peak, the SST drops
68 around sunset when outgoing turbulent heat fluxes and longwave radiation exceed the insolation
69 (Moulin et al. 2018), and thus induces nighttime convective mixing. The induced convective
70 mixing will then mix the surface mixed layer by destratifying the DWL and RL (Fig. 1c). It will
71 set the foundation SST (SST_{fnd} , which is closed to the nighttime minimum SST) similar with that
72 of the previous night.

73 Consecutive days of strong insolation and low wind speeds is one of the most important
74 features of the suppressed phase of MJO. This can result in the stratification of surface mixed
75 layer (e.g., Bernie et al. 2005; Moum et al. 2014) and generate higher daily-mean SST (Shinoda
76 and Hendon 1998; Bernie et al. 2005). The insolation captured in the DWL will be redistributed
77 through the deeper surface mixed layer by nighttime convective mixing. This heat can gradually
78 increase the SST_{fnd} and the stratification across the base of the DWL (Sui et al. 1997). In turn it
79 may suppress cold entrainment, allow SSTs to increase and through associated air-sea fluxes,
80 drive up the accumulation of atmospheric boundary layer heat and moisture for developing the
81 deep convection in MJOs (Zhang and Ling 2017)

82 The concept of an ocean barrier layer (BL) is first proposed (Lukas and Lindstrom 1991)
83 to identify the discrepancy between the surface mixed layer depth (MLD) and the top of seasonal
84 thermocline, mostly due to opposing salinity stratification. The BL is later defined as the layer
85 between the isothermal layer depth (ILD) and MLD (Sprintall and Tomczak 1992; McPhaden

86 and Foltz 2013; Chi et al. 2014). Strong precipitation may form a low-salinity layer near the sea
87 surface (as illustrated in Fig. 1d and h). The density stratification due to salinity will result in a
88 shallow MLD, while the temperature remains nearly homogenous (i.e., the definition of
89 isothermal layer IL) or even can be cooler at the surface compared to below (McPhaden and
90 Foltz 2013; Chi et al. 2014). The presence of salinity-based BL increases the required vertical
91 mixing to access the seasonal thermocline (Chi et al. 2014). On the other hand, the temporal
92 change of MLD is an useful indicator for identifying the strength of wind-driven mixing
93 (Balaguru et al. 2015), because the nighttime convective mixing cannot destratify the
94 temperature gradient in the seasonal thermocline abruptly. Thus, clearly salinity and temperature
95 gradients in the upper ocean are important to the dynamics of stratification and turbulent mixing.

96 Though the importance of DWL for inhibiting the turbulent mixing has been explored by
97 many previous studies (e.g., Moulin et al. 2018; Hughes et al. 2020), the thickness of DWL is
98 often estimated by finding the depth of an isotherm with high temperature (Matthews et al.
99 2014). However, because the density stratification modulated by the temperature structure can
100 affect the efficiency of turbulent mixing, exploring the factors to the extension of temperature
101 “gradient” in the DWL should be more crucial than focusing on the thickness of a high-
102 temperature layer. This study will discuss the evolution of temperature gradient above the MLD,
103 by using both the observations and model simulations during a strong DV SST event.

104 In November 2018, a collaborative field campaign between CSHOR and China’s First
105 Institution of Oceanography was conducted to explore the air-sea interaction in the Indonesian-
106 Australian Basin of the TWP (Feng et al. 2020). A shelf version of the Bailong buoy system
107 (Appendix A) was deployed off the northwest coast of Australia, along with six rapidly profiling
108 ALAMO floats from MRV Systems and two Teledyne Web EM-APEX floats. The observations

109 off Australia's Northwest Shelf collected during the suppressed phase of one MJO event around
110 the end of 2018 (Feng et al. 2020) will be reviewed in section 2. Definitions and the estimation
111 of different upper ocean stratified layers during diurnal warming will be described in section 3.
112 Results and discussions on SST variations and evolution of upper ocean layers will be presented
113 in sections 4 and 5, respectively. Section 6 will compare the observations with the model results
114 using the K-profile parameterization (KPP) of vertical mixing.

115

116 **2. ALAMO Float Measurements in the Field Experiment**

117 The field array was deployed at 115.3 °E and 16.8 °S on Nov 22nd 2018. Two ALAMO
118 floats (9206 and 9208) failed within two days of deployment. Floats 9205 and 9209 were
119 deployed at the southwest of floats 9207 and 9210. The distance between the floats was always
120 less than 50 km before Dec 5th. The remaining four ALAMO floats initially drifted
121 northwestward (Fig. 2). The floats except 9205 turned east since Dec 2nd, but still remained in a
122 cold filament whose SST ~ 26.5 °C. The drifting velocity of the floats is similar with the
123 satellite-measured geostrophic current (not shown in this study). That is, the float trajectories
124 should be mainly affected by the geostrophic currents of a strong cold-core cyclonic eddy located
125 just east of the float array, not the wind-driven current. No rains fell until the passage of an MJO
126 around the middle of December 2018 (Feng et al. 2020).

127 Two types of CTD sensors, Seabird SBE-41 (9207) and RBR (9205, 9206, 9208, 9209
128 and 9210), were mounted on the ALAMO floats. The floats continuously profiled the
129 temperature and salinity in the upper 600 m from Dec 1st to 5th 2018. Only the ascending profiles
130 are used for the analysis in this study, to avoid the CTD measurements being contaminated by

131 the wake effect. The time interval between ascending profiles was 3 to 4 h. The vertical
132 resolution of Seabird profiles was 1 m in the upper 50 m. The RBR sensors returned a vertical
133 resolution of 0.1 m in the upper 5 m, and 1 m from 5 to 50-m depth. We estimated the SST on
134 the RBR profiles by finding the peak temperature in the upper 1 m, often at ~ 0.2-m depth, after
135 excluding those with salinity measurements < 32 psu (which indicates air in the samples).
136 ALAMO floats also recorded the temperature during surface drift, when the pressure was less
137 than 0.2 dbar. Though the Seabird CTD sensors did not have the measurements in the upper 1 m,
138 the first surface value of temperature at about 0.1 or 0.2 dbar was always several degrees higher
139 than those reported at pressures < 0 dbar, similar with the typical difference between the air
140 temperature and SST in the region. Thus, we used the first surface value of temperature on the
141 Seabird surface reports as the SST at float 9207.

142 On Nov 28th 2018, the temperature in the upper 40 m at all four floats was about 26.3 °C
143 and is largely vertically mixed until Dec 1st (Fig. 3). The float-measured SST was ~ 0.2 °C
144 higher than the skin SST measured by the Himawari-8 satellites on Nov 30th (Fig. 2), consistent
145 with previous studies (Beggs et al. 2013). The SST measurements taken by Himawari-8 satellites
146 were described in appendix A. A strong DV SST event occurred between Dec 2nd and 4th (section
147 4), ~ 10 days before the passage of the deep convection in one MJO (often termed active phase;
148 Feng et al. 2020) arrived in the region. Except for float 9205, the temperature in the upper 40 m
149 increased up to 28 °C after Dec 3rd. Temperatures greater than 27 °C in the upper 40 m were then
150 sustained until the onset of the MJO's active phase around Dec 13th. Float 9205 measured
151 temperatures of > 26 °C down to 60-m depth on Dec 4th, deeper than that at the other three floats
152 at 40-m depth, while the salinity in the upper 40 m at float 9205 was higher than that at the other
153 floats by over 0.3 psu after Dec 2nd.

154

155 **3. Definitions of Upper Ocean Stratified Layers and DV SST**

156 Various criteria for estimating the depth of the MLD have been proposed (Sprintall and
157 Roemmich 1999; de Boyer Montégut et al. 2004; Suga et al. 2004), such as a temperature
158 difference that near the ocean surface (Wyrтки 1964) or density gradient criteria (Lukas and
159 Lindstrom 1991). Some studies estimate the MLD by finding the difference of potential density
160 $\Delta\rho$ between $\rho(\text{MLD})$ and $\rho(z_0)$ exceeding some arbitrary constant (e.g., $\Delta\rho = 0.1 \text{ kg m}^{-3}$ in Chi et
161 al. 2014), where z_0 is the reference depth closed to the ocean surface. The definition of z_0 is
162 required to exclude the unknown spikes of density gradient due to turbulence near the sea
163 surface.

164 A key question is, which z_0 is shallow enough to represent the “surface” value of $\rho(z_0)$
165 (Brainerd and Gregg 1995)? Different studies choose z_0 to avoid the impact of diurnal near
166 surface temperature stratification, e.g., $z_0 = 5 \text{ m}$ in McPhaden and Foltz (2013) or $z_0 = 10$ in de
167 Boyer Montégut et al. (2004), due to either an interest in longer timescales or limited vertical
168 observations. The daily development of temperature stratification in a DWL can complicate the
169 estimates of MLD (as the example in Fig. 1f), conflicting with the simple concept of a persistent
170 MLD at the top of seasonal thermocline. A more careful definition of z_0 needs to be used in the
171 presence of a DWL.

172

173 ***3.1 Depth of stratified layers in a diurnal cycle***

174 The absorption of insolation forms a DWL with strong temperature stratification in the
175 surface mixed layer, developing within a few hours of sunrise (Moulin et al. 2018). Here, the
176 diurnal warm layer depth is defined as the shallowest depth greater than 3 m (to avoid very near

177 surface turbulence) where vertical temperature gradients weaken to less than $0.02 \text{ }^\circ\text{C m}^{-1}$ over a
178 5-m span. That means temperature gradient is small below the DWL. This criterion focuses on
179 illuminating the roles of strong near surface temperature gradients (including the diurnal
180 thermocline) in stabilizing the upper ocean (Moulin et al. 2018), instead of the thickness of a
181 high-temperature layer (e.g., Matthews et al. 2014; section 5). In other word, in this study, a
182 “thicker” DWL occurs when a strong temperature gradient induced by the diurnal warming ($>$
183 $0.02 \text{ }^\circ\text{C m}^{-1}$) extends more deeply. The uncertainties of estimating DWL depth due to the choices
184 of the values of temperature gradient and spanning depth are studied in supporting information
185 A.

186 The MLD and ILD are estimated by using the estimated DWL as the reference depth z_0 .
187 We estimate the MLD by fulfilling two criteria at the same time: potential density difference $\Delta\rho$
188 $= \rho(\text{MLD}) - \rho(z_0) > 0.15 \text{ kg m}^{-3}$ (McPhaden and Foltz 2013) and potential density gradient $\partial\rho/\partial z$
189 $< -0.01 \text{ kg m}^{-4}$ (Brainerd and Gregg 1995), where the axis z is positive upward. The ILD is
190 estimated in the same way as the MLD (Chi et al. 2014), but using the temperature-dependent
191 profiles of ρ , which are computed assuming a constant salinity – here, the average of salinity in
192 the upper 5 m.

193

194 ***3.2 Temperature versus salinity-driven BL***

195 The barrier layer (BL) described by Lukas and Lindstrom (1991) exists due to salinity
196 stratification for driving the discrepancy between the MLD and ILD (Fig. 1d and h. McPhaden
197 and Foltz 2013; Chi et al. 2014). They also report a DWL near the ocean surface during the
198 daytime. Because the strong temperature stratification in the DWL stabilizes the upper ocean, the
199 effect of the DWL on vertical mixing (Moulin et al. 2018) can be similar to that of near surface

200 freshening (Smyth et al. 1997), and thus form a BL. Here, we will define a temperature-driven
201 BL (TBL) and salinity-driven BL (SBL). The TBL is identified if $DWL > 10$ m. The SBL is
202 identified if $ILD - MLD > 15$ m (see supporting information A for more details on the criteria).

203 Example profiles of salinity and temperature are used to illustrate the difference between
204 TBL and SBL (Fig. 4). A sharp diurnal thermocline with a temperature gradient extending to >
205 20-m depth, i.e., a thick DWL, is captured by float 9210 in the afternoon on Dec 2nd. Strong
206 density stratification in the TBL is due to the absorption of insolation. In comparison, at float
207 9209, the salinity stratification between 20 and 40-m depth around the 7am of Dec 3rd leads to
208 the separation of the ILD and MLD, due to a shallower SBL. The TBL and SBL (Chi et al. 2014)
209 driven by temperature and salinity stratification, respectively, may both increase the upper ocean
210 stratification, and thereby the threshold for the shear needed to induce vertical mixing.

211

212 *3.3 Magnitude of DV SST and foundation SST*

213 The Group for High Resolution Sea Surface Temperature (GHRSSST) defines the
214 foundation SST (SST_{fnd}) as the SST not affected by the diurnal variability, or the SST before
215 solar heat gain begins early in the day. Estimating the SST_{fnd} is difficult without using reliable
216 measurements of air-sea heat fluxes or models for predicting diurnal variation (Zhang et al.
217 2016). Several studies find the SST_{fnd} by averaging the nighttime SSTs before sunrise - from 12
218 to 5:30 am (Karagali and Høyer 2014; Zhang et al. 2016). Following this, we define SST_{fnd} as the
219 mean SST from 1 to 5 am. The magnitude of DV SST is then the difference between the SST_{fnd}
220 and following peak SST (SST_{max}).

221

222 4. SST Warming and Air-sea Heat Fluxes

223 We compute the SST_{fnd} and the magnitude of DV SST from Dec 1st to 4th 2018 (section
224 3), by using the float measurements of SST. On Dec 1st, the observed SST_{fnd} at all floats is
225 similar, ~ 26.4 °C, and reaches the peak (~ 26.9 °C) at around 3 - 4 pm. Compared with the
226 magnitude of DV SST reported by the previous studies (e.g., from 0.5 to 1.3 °C in Moulin et al.
227 2018), the magnitude of DV SST ~ 0.5 °C on Dec 1st is not extremely high (Fig. 5b-e). From Dec
228 2nd to 3rd, the significant DV SST > 2 °C occurs at all floats, termed a strong DV SST event in
229 this study. The highest SST of 29 °C occurs at the float 9209 on Dec 3rd.

230 Air-sea heat fluxes are computed (Fig. 6) using the atmospheric measurements from the
231 surface buoy and float-measured SST (supporting information B), based on the COARE 3.0
232 algorithm (Fairall et al. 1996a; Fairall et al. 2003). The trend of daily-mean air-sea net heat flux
233 is consistent with that of upper ocean heat storage rate. The latent (LH) plus sensible heat flux
234 (SH) drops from 220 to 80 W m^{-2} between Dec 1st and 3rd, because the wind speed decreases
235 down to 2 m s^{-1} (Fig. 5a). The peak of downward shortwave radiation before Dec 2nd is already $>$
236 900 W m^{-2} (appendix A), and low vertical shear of horizontal current is observed at the
237 surrounding EM-APEX float (not shown in this study), presumably due to the low wind speed.
238 That is, this strong DV SST event in the beginning of December mainly results from the
239 decreasing wind speed since Dec 1st, not increasing insolation.

240 The warming of SST_{fnd} varies significantly between each float from Dec 2nd to 4th (Fig.
241 5), even when their separation is less than 50 km. The SST_{fnd} at floats 9207 and 9210 increases
242 from 26.6 to 27.7 °C from Dec 2nd to 3rd in one day, right after the significant DV SST > 2 °C on
243 Dec 2nd. The SST_{fnd} at float 9209 increases from 26.4 to 27.6 °C between Dec 2nd and 4th. The

244 SST_{fld} at float 9205 is ~ 27 °C, smaller than the other three floats by 0.8 °C on Dec 4th. The
245 equivalent mean net heat flux at float 9205 is therefore ~ 8.4 W m⁻² lower than that at the floats
246 9207 and 9210 from Dec 2nd to 4th (Fig. 6).

247 On the other hand, though the LH is suppressed by the low wind speed from Dec 2nd to
248 4th, the SST_{fld} warming will eventually favor the LH once the wind speed increases (Hsu et al.
249 2019), e.g., the LH is up to -220 W m⁻² at wind speed > 6 m s⁻¹ on Dec 6th (not shown in this
250 study). The relative humidity rises to more than 80 % after Dec 7th as well (appendix A). In other
251 words, the warming of SST_{fld} in a short time period may largely enhance the “efficiency” for
252 accumulating of air-sea heat fluxes and moisture during the suppressed phase of MJOs (Maloney
253 2009).

254

255 **5. Upper Ocean Stratified Layers during Strong DV SST**

256 ***5.1 Evolution of DWL***

257 The strength of the ocean stratification is tracked through computing the Brunt-Väisälä
258 frequency N^2 ($=-(g/\rho)(\partial\rho/\partial z)$, where g is the gravity constant). The DWL is thin (< 10 m) on Dec
259 1st, associated with a small DV SST, ~ 0.5 °C. Starting from Dec 2nd, the solar insolation forms a
260 “thick” DWL as a TBL that extends its temperature gradient to more than 20-m depth, resulting
261 in strong density stratification ($N^2 > 1.0 \times 10^{-4} \text{ s}^{-2}$) near the ocean surface (Fig. 5). Note that the
262 criteria for estimating the DWL depend on only the temperature gradient. The extension of N^2
263 results from the vertical structure of temperature instead of salinity.

264 We further compare the estimates of DWL with the other definition of diurnal warm layer
265 DWL* (with the superscript *) in the aspect of a high-temperature layer. The DWL* can be found

266 at the depth of an isotherm in each day, whose temperature T^* equals to $\alpha \cdot SST_{\max} + (1-\alpha)SST_{\text{fnd}}$
267 or is at least $0.1 \text{ }^\circ\text{C}$ higher than the SST_{fnd} , assuming the $\alpha = 0.3$ (Matthews et al. 2014).
268 Considering the variations of SST_{\max} and SST_{fnd} between different days, the DWL^* can only be
269 used for comparing with the DWL in the individual day. During the strong DV SST event (Fig.
270 7), both DWL and DWL^* reach the peak in the evening or at the midnight (after 7 pm each day),
271 within several hours after the occurrence of SST_{\max} in the afternoon (~ 4 pm each day; section 4).
272 The turbulent diffusivity after the diurnal peak transports the warm water and extends the
273 temperature gradient to the deeper layer until the midnight. The DWL can be a reliable indicator
274 for identifying the strong DV SST in the consecutive days.

275 When the measured DV SST at all floats is $> 2 \text{ }^\circ\text{C}$ (Fig. 5), not only a thin layer with high
276 temperature is formed near the sea surface, a TBL with the significant extension of strong
277 temperature gradient also appears in the upper ocean. Interestingly, even the thin and high-
278 temperature ($\sim SST_{\max}$) layer within the upper 5 m disappears before 6 pm on Dec 3rd (Fig. 7),
279 the extension of temperature gradient in the DWL is not shoaled to < 5 m until the midnight of
280 Dec 4th. The deepening of DWL before the nighttime convective mixing may be induced by the
281 shear at the base of DWL (Matthews et al. 2014; Hughes et al. 2020). Because the density
282 stratification is affected by the temperature structure, the extension of temperature gradient
283 driven by the vertical shear (Hughes et al. 2020) may nonlinearly affect the turbulent diffusivity
284 above the MLD, and thereby the cooling of SST from the daytime peak.

285

286 ***5.2 Stratification above the MLD***

287 The MLD is estimated by using the DWL as the reference depth to avoid the temperature
288 gradient in the DWL (section 3). Because of the large N^2 below the MLD, the estimated MLD

289 captures the top of the seasonal thermocline reliably, ~ 50 m before Dec 2nd. Strong nighttime
290 convective mixing occurs above the MLD ($N^2 < 0$ shaded by the white color in Fig. 5), mainly
291 driven by latent heat flux and longwave cooling. During the strong DV SST event (section 4), the
292 MLD at the floats except 9205 is shoaled by 20 m, consistent with the change of SST_{fnd} from
293 26.6 to > 27.7 °C. At float 9205, the MLD and SST_{fnd} are nearly constant. Because the salinity at
294 float 9205 is higher than that at the other floats, we suspect that different vertical structure of
295 salinity between the floats may be associated with the variation of MLD shoaling.

296 Because the trajectories of the floats are slightly different, the measured vertical structure
297 of the salinity between the floats is not the same during the strong diurnal SST warming. On Dec
298 3rd, float 9209 measure a fresh-water layer with salinity ~ 34.4 psu near the sea surface. It results
299 in a SBL at 30-m depth during the diurnal warming. Because the simulated magnitude of DV
300 SST at float 9205 is still similar with the observation, the presence of SBL in the subsurface
301 layer may not affect the DV SST significantly.

302 Except at float 9205, the average of N^2 between 20 and 40-m depth (part of the surface
303 mixed layer on Dec 1st) increases from 5.0×10^{-5} to $1.0 \times 10^{-4} \text{ s}^{-2}$ from Dec 2nd to 4th. It shoals
304 the MLD by > 20 m. The restratification rate $\partial N^2 / \partial t$ is $\sim 3.5 \times 10^{-10} \text{ s}^{-3}$, much faster than that
305 reported by Brainerd and Gregg (1993a) during the daytime ($< 4 \text{ m s}^{-1}$ and peak insolation ~ 700
306 W m^{-2}), $\sim 1.6 \times 10^{-10} \text{ s}^{-3}$. The upper ocean becomes stably stratified in a few days. More
307 importantly, though the wind speed increases to $> 6 \text{ m s}^{-1}$ after Dec 5th, the MLD at floats 9207
308 and 9209 is still about 30 m, shallower than that at 50-m depth before Dec 2nd (Fig. 3). The
309 decrease of MLD agrees with the increase of SST_{fnd} from 26.5 °C to > 27 °C before and after the
310 strong DV SST event.

311 Clearly, the increase of SST_{fnd} is inversely proportional to the shoaling of MLD,
312 consistent with the model results reported by Bernie et al. (2005). The SST_{fnd} can be higher if the
313 same amount of heat content is accumulated in a shallower MLD. The shoaling of MLD also
314 coincidentally occurs after the strong DV $SST > 2$ °C except float 9205. Because the extension
315 of temperature gradient in the DWL can inhibit the vertical mixing efficiently, we speculate that
316 the thick DWL as a TBL may reduce the nighttime convective mixing for eroding the
317 stratification above the MLD. It prolongs the period for the penetrative solar radiation to
318 restratify the RL and shoal the MLD in the following day.

319 Despite of it, there may be some other factors for causing the restratification in the RL.
320 The role of penetrative solar radiation is studied in a one-dimensional model. The change of heat
321 absorption at different layers does not affect the density stratification below 30-m depth
322 significantly (section 6.2). The effect of horizontal advection is also studied. According to the
323 satellite measurements, the temperature advection at the sea surface may be insignificant near the
324 floats (supporting information C). However, without sufficient float measurements as direct
325 evidences, it is hard to quantify the temperature advection driven by the warm patch at 115 °E
326 and 15.3 °S (Fig. 2), and thereby the restratification of RL (Brainerd and Gregg 1993b). That is,
327 the cause of the rapid restratification of RL is still in doubt in this study. Understanding the
328 mechanism for changing the MLD is crucial for predicting the SST_{fnd} variations in the future.
329

330 **6. Simulations of SST Variations using the KPP mixing scheme**

331 The strong DV $SST > 2$ °C is observed at all ALAMO floats, associated with the
332 extension of temperature gradient in the DWL to the deeper layers (section 5). Can a numerical

333 model simulate the near surface temperature stratification we observed during these strong DV
334 SST events accurately? More importantly, which factors may be crucial for simulating the upper
335 ocean stratification during the diurnal warming? Compared with the multi-layer models such as
336 PWP3D (Price et al. 1986), the K-profile parameterization (KPP) can better simulate the DV
337 SST (Kawai and Wada 2007), and has been used in several ocean models (e.g., Shinoda and
338 Hendon 1998; Bernie et al. 2005). We will use the KPP in a one-dimensional Regional Oceanic
339 Modeling System (ROMS; Shchepetkin and McWilliams 2005) to simulate the evolution of
340 upper ocean stratification at the ALAMO array. Details of model settings and parameters in KPP
341 are described in appendix B.

342

343 *6.1 Simulated SST and density stratification N^2*

344 We compare the model, with a fine vertical resolution near the ocean surface (section
345 6.2), with the observations (Fig. 8a-d). On the first day of model simulations (Dec 1st), the KPP
346 simulated the SST reliably, including the DV SST of 0.5 °C. The simulated N^2 near the sea
347 surface is similar to that observed, as found in Bernie et al. (2005). After Dec 1st, the model still
348 predicts the SST at float 9205 well, including the SST_{\max} of 29 °C on Dec 3rd. At float 9209, the
349 simulated SST agrees with the observed SST well until the midnight of Dec 4th, i.e., before the
350 shoaling of MLD from 40 to 20-m depth. The model results of SST at floats 9207 and 9010
351 differ from the observations significantly since Dec 2nd, consistent with the timing of rapid
352 restratification in the RL.

353 The simulated temperature and salinity are used to compute the N^2 for discussing the
354 evolution of upper ocean stratified layers (Fig. 8). For the floats 9205 and 9209, which have the
355 similar MLD with the observations before Dec 4th, the simulated magnitude of DV SST agrees

356 with the observed DV SST. The occurrence of strong DV SST mainly results from the air-sea
357 heat fluxes in the one-dimensional process. Though the simulated SST_{\max} at floats 9207 and
358 9210 can still be $> 28\text{ }^{\circ}\text{C}$ on Dec 3rd, different N^2 above the MLD thereby SST_{fnd} results in the
359 discrepancy of SST between the model and observations. Even the KPP mixing scheme
360 simulates the DV SST magnitude and a highly stratified layer near the sea surface reliably, the
361 failure on predicting the stratification above MLD may affect the simulated SST_{fnd} thereby the
362 SST_{\max} .

363 On the other hand, compared with the observed DWL, the thickness of simulated DWL is
364 all less than 10 m, thinner than the observations after Dec 1st (Fig. 8e-1). The simulated N^2 in the
365 DWL ($> 1.0 \times 10^{-3}\text{ s}^{-2}$) is two times larger than the float measurements from 12 to 4 pm between
366 Dec 2nd and 4th. Most heat with high temperature gradient is accumulated near the sea surface in
367 the model, unlike the observed temperature gradient extending to the deeper layer. In other
368 words, though the magnitude of DV SST is similar, the structure of DWL between the model
369 results and observations can still differ significantly.

370

371 ***6.2 Effect of penetrative solar radiation on the RL's restratification***

372 Considering the importance of penetrative solar radiation for inducing diurnal warming
373 and restratifying the RL (Brainerd and Gregg 1993b), different coefficients based on five water
374 types are used in the parameterization of penetrative solar radiation (Paulson and Simpson 1978;
375 appendix B) during the model simulations (Fig. 9). The model results at float 9209 will be
376 discussed, because the SST difference at float 9209 between the model results and observations
377 is not significant until the warming of SST_{fnd} on Dec 4th. Before Dec 3rd, the DWL in the upper 5
378 m can be simulated by all model runs with different water types. The simulated magnitude of DV

379 SST is similar with the observation. On Dec 3rd, the simulation using the water type I forms a
380 shallower DWL with higher N^2 than the other water types. Because only the water type I has the
381 significant DV SST > 2 °C, the value of N^2 in the DWL may be the most dominant factor for
382 simulating the magnitude of DV SST.

383 Interestingly, the model results using the water type II or III have faster SST_{fnd} warming
384 from Dec 2nd to 4th (~ 0.7 °C) than those using other water types. Though their simulated N^2 in
385 the DWL is smaller than that in water type I, the N^2 in the DWL is not completely destratified by
386 the nighttime convective mixing since the midnight of Dec 3rd. The remaining N^2 in the water
387 types II and III implies that the simulated nighttime convective mixing may entrain less cold
388 water from the seasonal thermocline to the ocean surface than that in the water type I. That is, the
389 extension of temperature gradient to the deeper layer may more efficiently inhibit the nighttime
390 convective mixing in the model simulations. The evolution of upper ocean stratification,
391 including both DWL and MLD, is important to the forecast on the SST variations.

392

393 ***6.3 Effects of vertical resolution in the upper ocean***

394 Several previous studies discuss the importance for using the vertical resolution $\Delta z \leq 1$ m
395 in the simulation of DV SST (e.g., Bernie et al. 2005; Hughes et al. 2020). It may be sometimes
396 impractical to use the vertical resolution of 1 m in the entire ocean model for a climate forecast.
397 The effect of vertical resolution in different depth ranges of the upper ocean is thus studied by
398 using fine and coarse grids in the SST simulations, respectively, as detailed in Fig. 10a.

399 The difference of simulated SST_{max} (Fig. 10) between the fine and coarse grids is
400 negligible during the weak DV SST (e.g., Dec 1st and 2nd), but significant during the strong DV
401 SST (e.g., Dec 3rd). High vertical resolution in the upper 20 m may directly affect the

402 accumulated heat near the ocean surface for the SST warming, by simulating the detailed
403 structure of N^2 in the DWL, especially during the strong DV SST. The simulated SST_{fnd} in the
404 coarse grids is slightly warmer than that in the fine grids on Dec 4th, after the strong diurnal
405 warming on Dec 3rd. The Δz from 20 and 60-m depth may affect the simulated nighttime
406 convective mixing, and thereby the SST cooling from the daytime peak to the nighttime
407 minimum. Therefore, the Δz in the upper 20 m and from 20 and 60-m depth has a different
408 impact on the SST variation. The Δz in the upper 20 m may affect the simulated N^2 in the DWL
409 and SST_{max} in the afternoon. The Δz from 20 and 60-m depth may affect the simulations of the
410 nighttime convective mixing and SST_{fnd} .

411

412 ***6.4 Parameters in the KPP mixing scheme***

413 Because the KPP run with a high vertical resolution near the ocean surface fails to predict
414 the structure of DWL and rapid SST_{fnd} warming at three ALAMO floats (section 6.1), the values
415 of the mixing parameters in the K_p parameterizations are explored to seek improvements on the
416 simulations of SST_{fnd} at float 9209 (Fig. 11). We will discuss the parameters Ri_c and Ri_0
417 (appendix B), which directly affect the vertical diffusivity K_p within and below the OBL,
418 respectively.

419 Compared to the simulation using the default setting of mixing parameters ($Ri_c = 0.3$ and
420 $Ri_0 = 0.7$), decreasing the Ri_c from 0.3 to 0.1 (i.e., assuming the OBL is thinner) has negligible
421 effects to the simulated SST. Changing the thickness of the OBL may not affect the simulated
422 SST_{max} significantly, presumably due to the similar K_p below the OBL. On the other hand,
423 decreasing Ri_0 from 0.7 to 0.3 (i.e., more difficult for inducing shear instability) increases the
424 SST_{max} significantly, but has negligible effect on the SST_{fnd} . Inhibiting the vertical mixing by

425 restricting the depth range of K_p may affect the prediction of SST_{max} . If the Ri_0 alternatively
426 increases from 0.7 to 1 (i.e., larger depth ranges of K_p to transport heat at the base of OBL), the
427 KPP still fails to simulate the rapid SST_{fnd} warming. That is, the Ri_0 which affects the turbulent
428 diffusivity below the DWL is the most important parameter for the simulated DV SST magnitude
429 in the KPP.

430

431 7. Summary and Conclusion

432 Six ALAMO floats with high vertical resolution ≤ 1 m in the upper 50 m are deployed off
433 the northwest Australia on Nov 22nd 2018. Four floats measure strong DV SST of up to 2 °C in
434 the beginning of December, under low wind speed (~ 2 m s⁻¹) and sunny conditions. A rapid
435 SST_{fnd} warming is observed at three floats (9207, 9209 and 9210), rising from 26.4 to more than
436 27.6 °C between Dec 2nd and 4th. The increase of SST_{fnd} at float 9205 is ~ 0.5 °C, lower than that
437 at the other floats. The warming rate of SST_{fnd} varies significantly, even though the distance
438 between floats is less than 50 km. Because of the rapid SST_{fnd} warming, the latent plus sensible
439 heat flux at floats 9207 and 9210 is ~ 8.4 W m⁻² higher than that at float 9205 from Dec 2nd to 4th.

440 To emphasize the presence of a strong temperature gradient above the surface mixed
441 layer during the diurnal warming, a diurnal warm layer depth (DWL) is defined here by finding
442 the mean temperature gradient $\partial T/\partial z$ from z_0 to (z_0+5) -m depth > 0.02 °C m⁻¹. In other word, a
443 thick DWL will extend its strong temperature gradient to the deeper layer. Under the strong DV
444 SST ~ 2 °C, the averaged N^2 within the thick DWL (~ 20 m) is more than 1.0×10^{-4} s⁻². Below
445 the DWL, N^2 in the surface mixed layer increases from 5.0×10^{-5} to 1.0×10^{-4} from Dec 2nd to
446 4th. This restratification rate is faster than that reported by previous studies (e.g., Brainerd and

447 Gregg 1993a). This fast restratification below the DWL may prolong the period of high SST in
448 the tropical warm pool.

449 The KPP mixing scheme in a 1-D ROMS model is used to simulate the SST and upper
450 ocean stratified at the float positions. The simulated SST agrees well with the observed SST at
451 float 9205, including the strong DV SST > 2 °C. However, the model fails to simulate the rapid
452 SST_{fld} warming at the other three floats, presumably due to the other factors for simulating the
453 restratification above the MLD. Factors impacting the simulation of SST variations in the KPP
454 are discussed. High vertical resolution in the upper 20 m of < 1 m is required for reliably
455 simulating the magnitude of DV SST. Decreasing the mixing parameter Ri_0 for inhibiting the
456 turbulent diffusivity in the diurnal thermocline can directly increase the peak SST in the model
457 simulations. Changing the mixing parameter Ri_c has negligible effects to the SST simulations.

458 In summary, a stable sunny atmosphere with low wind speed is favorable for the
459 formation of a thick DWL during the suppressed phase of the MJOs. The extension of
460 temperature gradient in the DWL is studied using the high vertical resolution measurements in
461 the first time, and can be more than 20 m during the strong DV SST > 2 °C. The shoaling of
462 MLD can also increase the SST_{fld}. Though the KPP mixing scheme can simulate the DV SST
463 magnitude reliably by using high vertical resolution near the sea surface, it fails to predict the
464 increase SST_{fld}, mainly due to different upper ocean density structure between the model and
465 observations. Questions still remain regarding to the factors for shoaling the observed MLD in a
466 short time period. Future field measurements on turbulent diffusivity within the DWL in TWPs
467 are important for improving the ocean mixing approaches in the global coupled models for the
468 MJO forecast.

469

470 **Acknowledgments**

471 This work is funded by the project of “Coupled warm pool dynamics in the Indo-Pacific” under
472 the Centre for Southern Hemisphere Oceans Research (CSHOR). CSHOR is a joint initiative
473 between the Qingdao National Laboratory for Marine Science and Technology (QNLN),
474 CSIRO, University of New South Wales and University of Tasmania. The authors thank Dr.
475 Beggs for advising the product of SST measured by the Himawari-8 satellite, the IMOS portal
476 for processing the dataset of sea surface height anomalies in the dataset “IMOS - OceanCurrent -
477 Gridded sea level anomaly - Delayed mode” (<https://portal.aodn.org.au/>), N. Bogue and R.
478 Nigash at MRV for helping configure and pilot the floats, D. Slawinski (CSIRO) and P. Robbins
479 (WHOI) for post-processing the float measurements. Float data is stored at
480 <https://doi.org/10.25919/5da51c424add0>.

481

482 **Appendix A. Buoy and Satellite Measurements**

483 The Bailong buoy system from the First Institution of Oceanography (Cole et al. 2011)
484 includes the atmospheric measurements near the ocean surface (Fig. 12) and subsurface ocean
485 measurements in the upper 500 m (Feng et al. 2020). The atmosphere data is sampled in every 10
486 minutes. During the strong DV SST event from Dec 2nd to 4th 2018, the peak insolation is more
487 than 1000 W m^{-2} , and the wind speed at 4-m height above the sea surface is about 2 m s^{-1} . Strong
488 diurnal variation of air temperature is found, $\sim 1 \text{ }^\circ\text{C}$ on Dec 2nd. The relative humidity (RH) is
489 about 60%, and then increases until the onset of the MJO. The temporal variation of downward
490 longwave radiation is small, from 400 to 450 W m^{-2} .

491 The infrared sensor mounted on the Japanese geostationary Himawari-8 satellite
492 measures the skin SST in four spectral bands (8.59, 10.40, 11.24 and $12.38 \text{ }\mu\text{m}$) for every 10
493 minutes with the horizontal resolution $< 2 \text{ km}$ (Kramar et al., 2016). The product of Himawari-8
494 SST reprocessed by Dr. Christopher Griffin
495 ([http://opendap.bom.gov.au:8080/thredds/catalog/abom_imos_ghrsst_archive-](http://opendap.bom.gov.au:8080/thredds/catalog/abom_imos_ghrsst_archive-1/v02.0fv03test/Continental/L3C-01hour/ABOM-L3C_GHRSST-SSTskin-AxIH08/2018/)
496 [1/v02.0fv03test/Continental/L3C-01hour/ABOM-L3C_GHRSST-SSTskin-AxIH08/2018/](http://opendap.bom.gov.au:8080/thredds/catalog/abom_imos_ghrsst_archive-1/v02.0fv03test/Continental/L3C-01hour/ABOM-L3C_GHRSST-SSTskin-AxIH08/2018/)) in
497 Bureau of Meteorology Australia as an hourly dataset is available online. We also use the near-
498 real time sea surface height anomalies data processed by Integrated Marine Observing System
499 (IMOS) data portal (Baird and Ridgway 2012; Deng et al. 2010), to understand the distribution
500 of eddies around floats. The geostrophic current is computed, mostly northward and $< 0.2 \text{ m s}^{-1}$
501 along the trajectories of floats.

502

503 **Appendix B. KPP Mixing Scheme in the 1-D ROMS Model Simulation**

504 ***B.1. ROMS model description***

505 The one-dimensional ROMS model with the KPP mixing is used to simulate the SST
506 warming at each ALAMO floats. The atmosphere measurements taken by the FIO buoys,
507 including insolation, downward longwave radiation, air temperature, air pressure, atmosphere
508 wind and relative humidity, are used as the forcing at the floats, by assuming the spatial variation
509 of atmosphere condition negligible within the distance of 80 km. The temporal resolution is 10
510 min. The profiles at each float from 9 to 11 pm on Nov 30th are averaged as the initial conditions.

511 We use the parameterization of penetrative solar radiation Q proposed by Paulson and
512 Simpson (1977) for simulating the change of upper ocean stratification, which can be expressed
513 as

$$514 \quad Q = Q_0 \left(r \exp\left(\frac{z}{\mu_1}\right) + (1 - r) \exp\left(\frac{z}{\mu_2}\right) \right) \quad (S2)$$

515 where Q_0 is the insolation, r , μ_1 and μ_2 are the coefficients based on the data of five different
516 water types in Jerlov (1976) (**Error! Reference source not found.**;
517 <https://www.myroms.org/wiki/Jwtype>). According to the description in the ROMS model,
518 water type I is used for open Pacific Ocean; water type IA is used for open Indian Ocean; water
519 type IB is used for open Atlantic Ocean; water type II is used for Azores; water type III is used
520 for North Sea. Most model results are simulated using the coefficients of water type I, except
521 those in section 6.2.

522

523 ***B.2. KPP mixing scheme***

524 The K-profile parameterization (KPP, Large et al. 1994) used in many ocean models,
525 such as HYbrid Coordinate Ocean Model (HYCOM; Chassignet et al. 2007), computes the
526 turbulent diffusivity by assuming a shape function in the OBL. It differs to the turbulence kinetic
527 energy (TKE) closure scheme (e.g., Mellor and Yamada 1982), which uses a prognostic TKE
528 energy equation and length scale of mixing.

529 In the KPP mixing scheme, after prescribing the surface forcing, the depth h of ocean
530 boundary layer (OBL) will be first determined by using a critical bulk Richardson number Ri_c
531 (default = 0.3). The diffusivity in the OBL, K_{Ric} , is computed based on the surface flux and h ,
532 assuming a nondimensional vertical shape function. For the diffusivity below the OBL, K_{Ri0} , the
533 shear instability mixing occurs only when the local gradient Richardson number Ri is smaller
534 than a critical gradient Richardson number Ri_0 (default = 0.7). The total diffusivity K_p is
535 constituted by the K_{Ric} , K_{Ri0} and background diffusivity K_{p0} (default = 1.0×10^{-6}).

536

537

538

539

540

541

542 **References**

- 543 Baird, M. E., and K. R., Ridgway, 2012. The southward transport of sub-mesoscale lenses of
544 Bass Strait Water in the centre of anti-cyclonic mesoscale eddies, *Geophysical Research*
545 *Letter*, 39, L02603, doi:10.1029/2011GL050643.
- 546 Balaguru, K., G. R., Foltz, L. R. , Leung, E., D'Asaro, K. A. , Emanuel, H. , Liu, and S. E.,
547 Zedler, 2015. Dynamic Potential Intensity: An improved representation of the ocean's
548 impact on tropical cyclones, *Geophysical Research Letter*, 42, 6739– 6746,
549 doi:10.1002/2015GL064822.
- 550 Beggs, H., L., Majewski, G., Kruger, R., Verein, P., Oke, P., Sakov, X., Huang, L., Garde and C.
551 Tingwell, 2013. Report to GHRSSST14 from Australia — Bluelink and IMOS.
552 [http://imos.org.au/fileadmin/user_upload/shared/SRS/Beggs_Australian_Report_GHR](http://imos.org.au/fileadmin/user_upload/shared/SRS/Beggs_Australian_Report_GHR_SST14_10Dec2013.pdf)
553 [SST14_10Dec2013.pdf](http://imos.org.au/fileadmin/user_upload/shared/SRS/Beggs_Australian_Report_GHR_SST14_10Dec2013.pdf)
- 554 Bellenger, H. and J. Duvel, 2009. An Analysis of Tropical Ocean Diurnal Warm Layers. *J.*
555 *Climate*. 22, 3629–3646. <https://doi.org/10.1175/2008JCLI2598.1>
- 556 Bernie, D. J., S. J. Woolnough, J. M. Slingo, and E. Guilyardi, 2005. Modeling Diurnal and
557 Intraseasonal Variability of the Ocean Mixed Layer, *Journal of Climate*, 18, 1190-1202.
- 558 Bernie, D. J., E. Guilyardi, G. Madec, J. M. Slingo, S. J. Woolnough and J. Cole, 2008. Impact
559 of resolving the diurnal cycle in an ocean–atmosphere GCM. Part 2: A diurnally coupled
560 CGCM. *Climate Dynamics*, 31, 909-925, doi: 10.1007/s00382-008-0429-z
- 561 Brainerd, K. E. and M. C. Gregg, 1993a. Diurnal restratification and turbulence in the oceanic
562 surface mixed layer: 1. Observations. *Journal of Geophysical Research: Oceans*, 98, 22645-
563 22656, doi:10.1029/93JC02297.

564 Brainerd, K. E., and M. C. Gregg, 1993b. Diurnal restratification and turbulence in the oceanic
565 surface mixed layer: 2. Modeling, *Journal of Geophysical Research*, 98, 22657– 22664,
566 doi:10.1029/93JC02298.

567 Brainerd, K. E., and M. C. Gregg, 1995. Surface mixed and mixing layer depths, *Deep Sea*
568 *Research Part I: Oceanographic Research Papers*, 42, 1521-1543.

569 Caldwell, D. R., R.-C. Lien, J. N. Moum, and M. C. Gregg, 1997. Turbulence decay and
570 restratification in the equatorial ocean surface layer following nighttime convection. *Journal*
571 *of Physical Oceanography*, 27, 1120–1132.

572 Chassignet, E. P., H. E., Hurlburt, O. M., Smedstad, G. R., Halliwell, P. J., Hogan, A. J.,
573 Wallcraft, R., Baraille and R., Bleck, 2007. The HYCOM (HYbrid Coordinate Ocean
574 Model) data assimilative system. *Journal of Marine Systems* 65, pp. 60-83. doi:
575 <https://doi.org/10.1016/j.jmarsys.2005.09.016>

576 Chi, N.-H., R.-C. Lien, E. A. D'Asaro and B. B. Ma, 2014. The surface mixed layer heat budget
577 from mooring observations in the central Indian Ocean during Madden–Julian Oscillation
578 events. *Journal of Geophysical Research: Oceans*. 119, 4638– 4652,
579 doi:10.1002/2014JC010192.

580 Cole, R., J. Kinder, Chun Lin Ning, W. Yu and Yang Chao, "'Bai-Long": A TAO-hybrid on
581 RAMA," *OCEANS'11 MTS/IEEE KONA*, Waikoloa, HI, 2011, pp. 1-10. doi:
582 10.23919/OCEANS.2011.6106952

583 Cronin, M. F., and McPhaden, M. J., 1998. Upper ocean salinity balance in the western
584 equatorial Pacific, *Journal of Geophysical Research*, 103, 27567– 27587,
585 doi:10.1029/98JC02605.

586 de Boyer Montégut, C., G., Madec, A. S., Fischer, A., Lazar, and D. Iudicone, 2004. Mixed layer
587 depth over the global ocean: An examination of profile data and a profile-based
588 climatology, *Journal of Geophysical Research*, 109, C12003, doi:10.1029/2004JC002378.

589 DeMott, C. A., N. P. Klingaman, and S. J. Woolnough, 2015. Atmosphere-ocean coupled
590 processes in the Madden-Julian oscillation, *Reviews of Geophysics*, 53, 1099-1154.

591 Deng, X, D. A. Griffin, K. Ridgway, J.A. Church, W.E. Featherstone, N. White and M. Cahill,
592 2010. Satellite altimetry for geodetic, oceanographic and climate studies in the Australian
593 region, in: Vignudelli S., A. Kostianoy, and P. Cipollini and J. Benveniste (eds.), *Coastal*
594 *Altimetry*, Springer-Verlag, Berlin. ISBN: 978-3-642-12795-3. e-ISBN: 978-3-642-12796-
595 0. doi: 10.1007/978-3-642-12796-0_18

596 Drushka, K., S. T. Gille and J. Sprintall, 2014. The diurnal salinity cycle in the tropics. *Journal of*
597 *Geophysical Research: Oceans*, 119, 5874-5890, doi: 10.1002/2014jc009924

598 Drushka, K., W., Asher, A., Jessup, E., Thompson, S., Iyer, D., Clark, 2019. Capturing Fresh
599 Layers with the Surface Salinity Profiler. *Oceanography*. 32. 76-85.
600 10.5670/oceanog.2019.215.

601 Fairall, C. W., E. F., Bradley, D. P., Rogers, J. B., Edson, and G. S., Young, 1996a. Bulk
602 parameterization of air-sea fluxes for Tropical Ocean-Global Atmosphere Coupled-Ocean
603 Atmosphere Response Experiment, *Journal of Geophysical Research*, 101, 3747– 3764,
604 doi:10.1029/95JC03205.

605 Fairall, C. W., E. F., Bradley, J. S., Godfrey, G. A., Wick, J. B., Edson, and G. S. Young, 1996b.
606 Cool-skin and warm-layer effects on sea surface temperature, *J. Geophys. Res.*, 101, 1295–
607 1308, doi:10.1029/95JC03190.

608 Fairall, C.W., E. F. Bradley, J. E. Hare, A. A. Grachev, and J. B. Edson, 2003. Bulk
609 Parameterization of Air-Sea Fluxes: Updates and Verification for the COARE Algorithm. *J.*
610 *Climate*, 16, pp 571-591.

611 Feng, M., Y., Duan, S., Wijffels, J.-Y., Hsu, C., Li, H., Wang, Y., Yang, H., Shen, J., Liu, C.,
612 Ning, and W., Yu, 2020. Tracking air-sea exchange and upper ocean variability in the
613 Southeast Indian Ocean during the onset of the 2018-19 Australian summer monsoon.
614 *Bulletin of the American Meteorological Society*. [https://doi.org/10.1175/BAMS-D-19-](https://doi.org/10.1175/BAMS-D-19-0278.1)
615 [0278.1](https://doi.org/10.1175/BAMS-D-19-0278.1).

616 Gargett, A. E., and G. Holloway, 1984. Dissipation and diffusion by internal wave breaking,
617 *Journal of Marine Research*, **42**, 15-27

618 Guilyardi, E., 2006. El niño-mean state-seasonal cycle interactions in a multi-model ensemble.
619 *Climate Dynamics*. 26. 329–348

620 Hsu, J.-Y., H., Hendon, M., Feng, and X., Zhou, 2019. Magnitude and phase of diurnal SST
621 variations in the ACCESS-S1 model during the suppressed phase of the MJOs. *Journal of*
622 *Geophysical Research: Oceans*, 124, 9553– 9571. <https://doi.org/10.1029/2019JC015458>

623 Hughes, K. G., J. N. Moum and E. L. Shroyer, 2020. Evolution of the Velocity Structure in the
624 Diurnal Warm Layer. *Journal of Physical Oceanography*, 50, 615-631, doi: 10.1175/jpo-d-
625 19-0207.1

626 Jerlov, N. G., 1976. *Marine Optics*, 14, Elsevier Oceanography Series

627 Karagali, I., and Høyer, J. L., 2014. Characterisation and quantification of regional diurnal SST
628 cycles from SEVIRI. *Ocean Science*, 10, 745–758. [http://dx.doi.org/10.5194/os- 10-745-](http://dx.doi.org/10.5194/os-10-745-2014)
629 [2014](http://dx.doi.org/10.5194/os-10-745-2014).

630 Kawai, Y. and Wada, A., 2007. Diurnal sea surface temperature variation and its impact on the
631 atmosphere and ocean: A review. *Journal of Oceanography*, 63, 721-744, doi:
632 10.1007/s10872-007-0063-0

633 Kramar, M., A. Ignatov, B. Petrenko, Y. Kihai, P. Dash, 2016. Near real time SST retrievals
634 from Himawari-8 at NOAA using ACSPO system. *Proc. SPIE 9827, Ocean Sensing and*
635 *Monitoring*.

636 Kudryavtsev, V.N. and A.V. Soloviev, 1990. Slippery Near-Surface Layer of the Ocean Arising
637 Due to Daytime Solar Heating. *Journal of Physical Oceanography*, 20, 617–628,
638 [https://doi.org/10.1175/1520-0485\(1990\)020<0617:SNSLOT>2.0.CO;2](https://doi.org/10.1175/1520-0485(1990)020<0617:SNSLOT>2.0.CO;2)

639 Kunze, E., 2003. A review of oceanic salt-fingering theory. *Progress in Oceanography*, 56, 399-
640 417. doi: [https://doi.org/10.1016/S0079-6611\(03\)00027-2](https://doi.org/10.1016/S0079-6611(03)00027-2)

641 Large, W. G., J. C. McWilliams, and S. C. Doney, 1994. Oceanic vertical mixing: A review and
642 a model with a nonlocal boundary layer parameterization, *Reviews of Geophysics*, 32, 363-
643 403.

644 Lee, C., K.-I., Chang, J. H., Lee, and K. J., Richards, 2014. Vertical mixing due to double
645 diffusion in the tropical western Pacific, *Geophysical Research Letter*, 41, 7964– 7970,
646 doi:10.1002/2014GL061698.

647 Lukas, R., and E. Lindstrom, 1991. The mixed layer of the western equatorial Pacific Ocean, *J.*
648 *Geophys. Res.*, 96(S01), 3343– 3357, doi:10.1029/90JC01951.

649 Maloney, E. D., 2009. The Moist Static Energy Budget of a Composite Tropical Intraseasonal
650 Oscillation in a Climate Model, *Journal of Climate*, 22, 711-729.

651 Matthews, A.J., D.B. Baranowski, K.J. Heywood, P.J. Flatau, and S. Schmidtko, 2014. The
652 Surface Diurnal Warm Layer in the Indian Ocean during CINDY/DYNAMO. *Journal of*
653 *Climate*, 27, 9101–9122, <https://doi.org/10.1175/JCLI-D-14-00222.1>

654 McPhaden, M. J. and G. R. Foltz, 2013. Intraseasonal variations in the surface layer heat balance
655 of the central equatorial Indian Ocean: The importance of zonal advection and vertical
656 mixing. *Geophysical Research Letters*. 40, 2737– 2741, doi:10.1002/grl.50536.

657 Mellor, G. L., and T. Yamada, 1982. Development of a turbulence closure model for geophysical
658 fluid problems, *Rev. Geophys.*, 20, 851– 875, doi:10.1029/RG020i004p00851.

659 Moulin, A. J., J. N. Moum and E. L. Shroyer, 2018. Evolution of Turbulence in the Diurnal
660 Warm Layer. *Journal of Physical Oceanography*, 48, 383-396, doi: 10.1175/jpo-d-17-0170.1

661 Moum, J. N., S. P. de Szoeke, W. D. Smyth, J. B. Edson, H. L. DeWitt, A. J. Moulin, E. J.
662 Thompson, C.J. Zappa, S. A. Rutledge, R. H. Johnson, and C. W. Fairall, 2014. Air–Sea
663 Interactions from Westerly Wind Bursts During the November 2011 MJO in the Indian
664 Ocean. *Bull. Amer. Meteor. Soc.*, 95, 1185–1199, [https://doi.org/10.1175/BAMS-D-12-](https://doi.org/10.1175/BAMS-D-12-00225.1)
665 [00225.1](https://doi.org/10.1175/BAMS-D-12-00225.1)

666 Paulson, C. A., and J. J. Simpson, 1977. Irradiance measurements in the upper ocean, *Journal of*
667 *Physical Oceanography*, 7, 952-956.

668 Price, J. F., R. A. Weller and R. Pinkel, 1986. Diurnal cycling: Observations and models of the
669 upper ocean response to diurnal heating, cooling, and wind mixing. *Journal of Geophysical*
670 *Research: Oceans*, 91, 8411-8427, doi: 10.1029/JC091iC07p08411

671 Ruppert, J. H., and R. H. Johnson, 2015. Diurnally modulated cumulus moistening in the
672 preonset stage of the Madden-Julian oscillation during DYNAMO, *Journal of the*
673 *Atmospheric Sciences*, 72, 1622–1647.

674 Seo, H., A. C. Subramanian, A. J. Miller, and N. R. Cavanaugh, 2014. Coupled Impacts of the
675 Diurnal Cycle of Sea Surface Temperature on the Madden–Julian Oscillation, *Journal of*
676 *Climate*, 27, 8422-8443, <https://doi.org/10.1175/JCLI-D-14-00141.1>

677 Shchepetkin, A. F., and J. C. McWilliams, 2005. The regional oceanic modeling system (ROMS)
678 a split-explicit, free-surface, topography-following-coordinate oceanic model. *Ocean*
679 *Modelling*, 9, pp. 347-404.

680 Shinoda, T. and H. H. Hendon, 1998. Mixed Layer Modeling of Intraseasonal Variability in the
681 Tropical Western Pacific and Indian Oceans. *Journal of Climate*, 11, 2668–2685,
682 [https://doi.org/10.1175/1520-0442\(1998\)011<2668:MLMOIV>2.0.CO;2](https://doi.org/10.1175/1520-0442(1998)011<2668:MLMOIV>2.0.CO;2)

683 Shinoda, T., T. G. Jensen, M. Flatau, and S. Chen, 2013. Surface Wind and Upper-Ocean
684 Variability Associated with the Madden–Julian Oscillation Simulated by the Coupled
685 Ocean–Atmosphere Mesoscale Prediction System (COAMPS), *Monthly Weather Review*,
686 141, 2290-2307.

687 Sobel, A., S. Wang, and D. Kim, 2014. Moist Static Energy Budget of the MJO during
688 DYNAMO, *Journal of the Atmospheric Sciences*, 71, 4276-4291.

689 Soloviev, A., and R., Lukas, 2006. *The near-surface layer of the Ocean*. Springer.

690 Sprintall, J., and M. Tomczak, 1992. Evidence of the barrier layer in the surface layer of the
691 tropics, *J. Geophys. Res.*, 97, 7305– 7316, doi:10.1029/92JC00407.

692 Sprintall, J., and D. Roemmich, 1999. Characterizing the structure of the surface layer in the
693 Pacific Ocean, *J. Geophys. Res.*, 104, 23,297–23,311.

694 Suga, T., K. Motoki, Y. Aoki, and A. M. Macdonald, 2004. The North Pacific climatology of
695 winter mixed layer and mode waters, *Journal of Physical Oceanography*, 34, 3–22.

696 Sui, C., X. Li, K. Lau, and D. Adamec, 1997. Multiscale Air–Sea Interactions during TOGA
697 COARE. *Monthly Weather Review*, 125, 448–462, [https://doi.org/10.1175/1520-
698 0493\(1997\)125<0448:MASIDT>2.0.CO;2](https://doi.org/10.1175/1520-0493(1997)125<0448:MASIDT>2.0.CO;2)

699 Sutherland, G., L. Marié, G. Reverdin, K.H. Christensen, G. Broström, and B. Ward, 2016.
700 Enhanced Turbulence Associated with the Diurnal Jet in the Ocean Surface Boundary
701 Layer. *Journal of Physical Oceanography*, 46, 3051–3067, [https://doi.org/10.1175/JPO-D-
702 15-0172.1](https://doi.org/10.1175/JPO-D-15-0172.1)

703 Vijith, V., P. N. Vinayachandran, B. G. M. Webber, A. J. Matthews, J. V. George, V. K.
704 Kannaujia, A. A. Lotliker and P. Amol, 2020. Closing the sea surface mixed layer
705 temperature budget from in situ observations alone: Operation Advection during BoBBLE.
706 *Scientific Reports*, 10, pp. 7062, doi: <https://doi.org/10.1038/s41598-020-63320-0>

707 Wyrтки, K., 1964. The thermal structure of the eastern Pacific Ocean, *Deutsche hydrographische*
708 *Zeitschrift*, 8, 6-84

709 Zhang, C., 2005. Madden-Julian Oscillation, *Reviews of Geophysics*, 43, RG2003,
710 doi:10.1029/2004RG000158.

711 Zhang, H., H. Beggs, L. Majewski, X. H. Wang, and A. Kiss, 2016. Investigating sea surface
712 temperature diurnal variation over the Tropical Warm Pool using MTSAT-1R data, *Remote*
713 *Sensing of Environment*, 183, 1-12.

714 Zhang, C. and J. Ling, 2017. Barrier Effect of the Indo-Pacific Maritime Continent on the MJO:
715 Perspectives from Tracking MJO Precipitation. *Journal of Climate*, 30, 3439–3459,
716 <https://doi.org/10.1175/JCLI-D-16-0614.1>

717 Zhao, Z., 2018. The global mode-2 M2 internal tide. *Journal of Geophysical Research: Oceans*,
718 123, 7725–7746. <https://doi.org/10.1029/2018JC014475>

719

720

721

722

723

724 **Table**

	Water Types				
	I	IA	IB	II	III
r	0.58	0.62	0.67	0.77	0.78
μ_1	0.35	0.60	1.00	1.50	1.40
μ_2	23.00	20.00	17.00	14.00	7.90

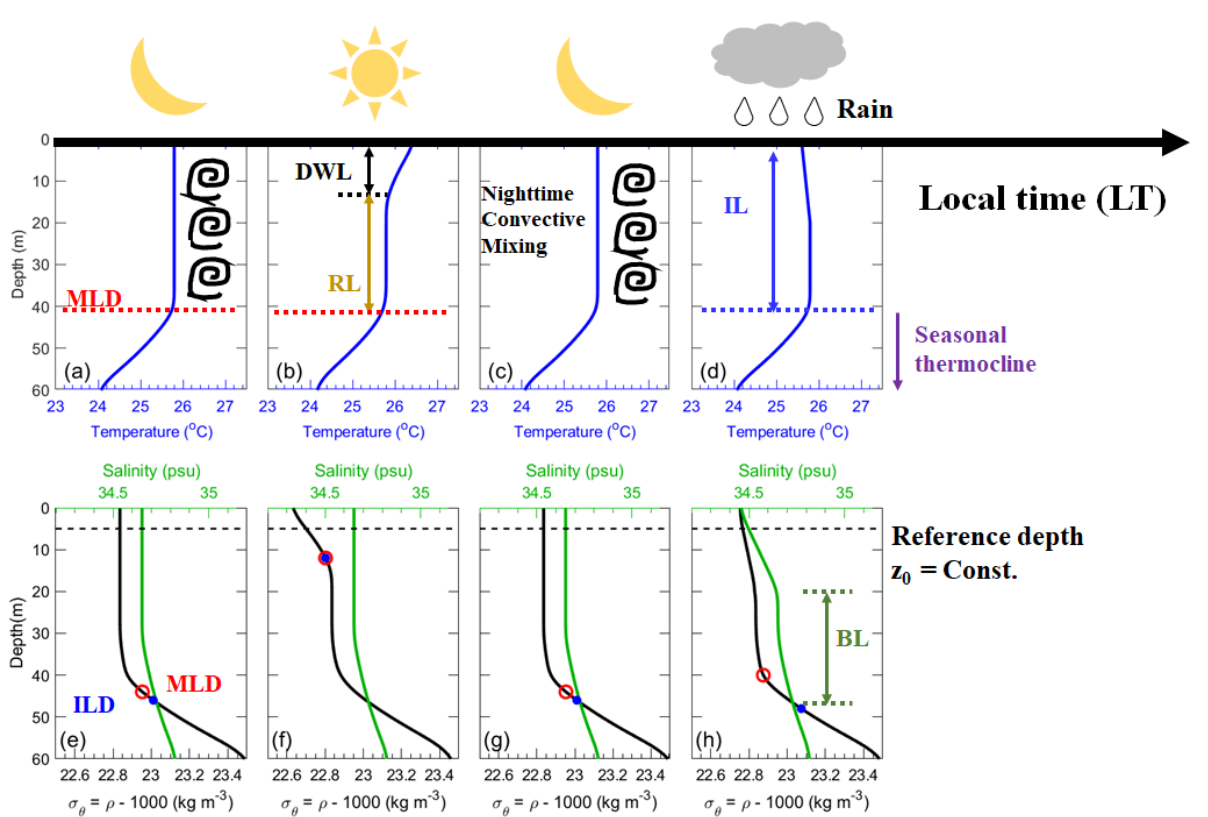
725

726 Table. 1. The coefficients used in the parameterization of penetrative solar radiation (Eq. S2)

727 based on the data of five different water types reported by Jerlov (1976).

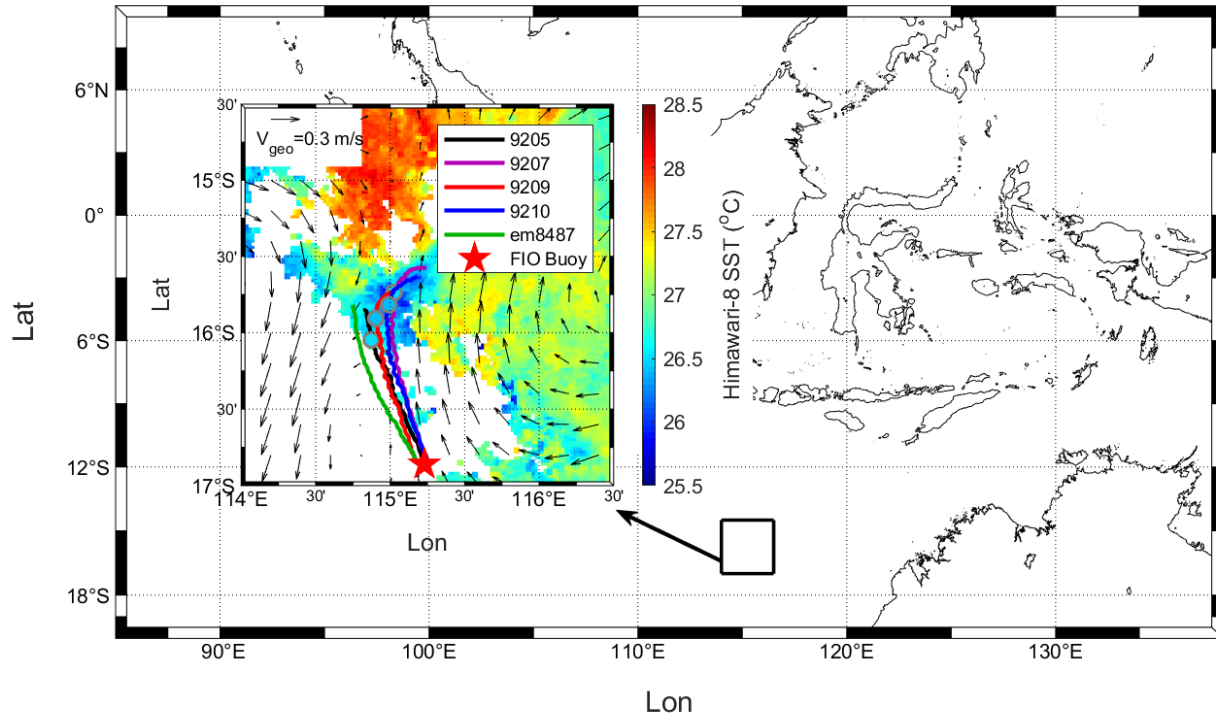
728

729 **Figure**
 730



731
 732 Fig. 1. Illustration on the surface mixed layer depth (MLD), diurnal warm layer (DWL), remnant
 733 layer (RL), isothermal layer (IL) and barrier layer (BL), using assumed temperature (blue lines in
 734 a-d) and salinity profiles (green lines in e-h). The RL exists between the DWL and MLD.
 735 Examples of estimating MLD and ILD based on the criteria used in the previous studies are
 736 presented in (e)-(h). The MLD (red circles) is estimated when the potential density difference
 737 $\rho(\text{MLD}) - \rho(z_0) > 0.1 \text{ kg m}^{-3}$ (Chi et al. 2014), assuming the constant reference depth z_0 at 5-m
 738 depth (black dashed lines in e-h). The isothermal layer depth (ILD. Blue dots) is estimated in the
 739 same way as the MLD but using temperature-dependent profiles of ρ , which assumes the salinity
 740 as the mean in the upper 5-m ocean. The formation of BL (difference between MLD and ILD >
 741 20 m) is due to the precipitation freshening the salinity in the upper 20 m, and is regarded as the

742 salinity-driven barrier layer (SBL) in section 3. The temperature near the sea surface in (d) is
743 slightly cooled by rains (Druksha et al. 2019).

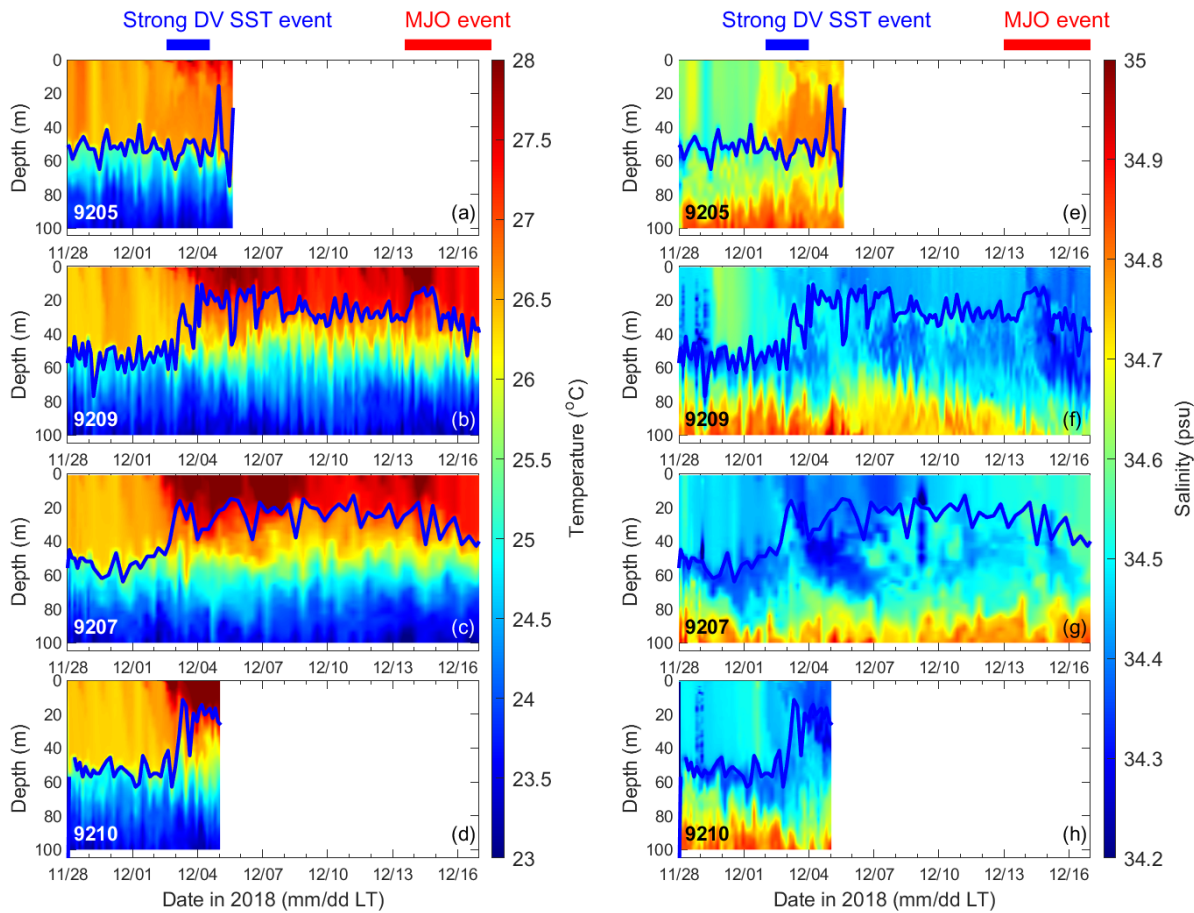


744

745 Fig. 2. Trajectories of four ALAMO floats (color lines) and one EM-APEX float (green line) in
 746 the map of SST (color shading) measured by Himawari-8 satellite (appendix A) within the region
 747 of TWP (black box in the big map) around 12 am on Dec 1st 2018. The ALAMO floats and EM-
 748 APEX floats were deployed near the FIO buoy (red pentagram) at 115.3 °E and 16.8 °S in the
 749 northwest Australia on Nov 22nd, and drifting northwestward (color lines are trajectories from
 750 Nov 22nd to Dec 6th 2018) due to the geostrophic current (black arrows in the small map, and
 751 their magnitude can be referenced to that on the upper-left corner). The color dots connected to
 752 the ALAMO float trajectories are the float-measured SST around the midnight of Dec 1st 2018.
 753 The geostrophic current V_{geo} is estimated using the IMOS sea surface height anomalies on Dec
 754 1st 2018 (appendix A).

755

756



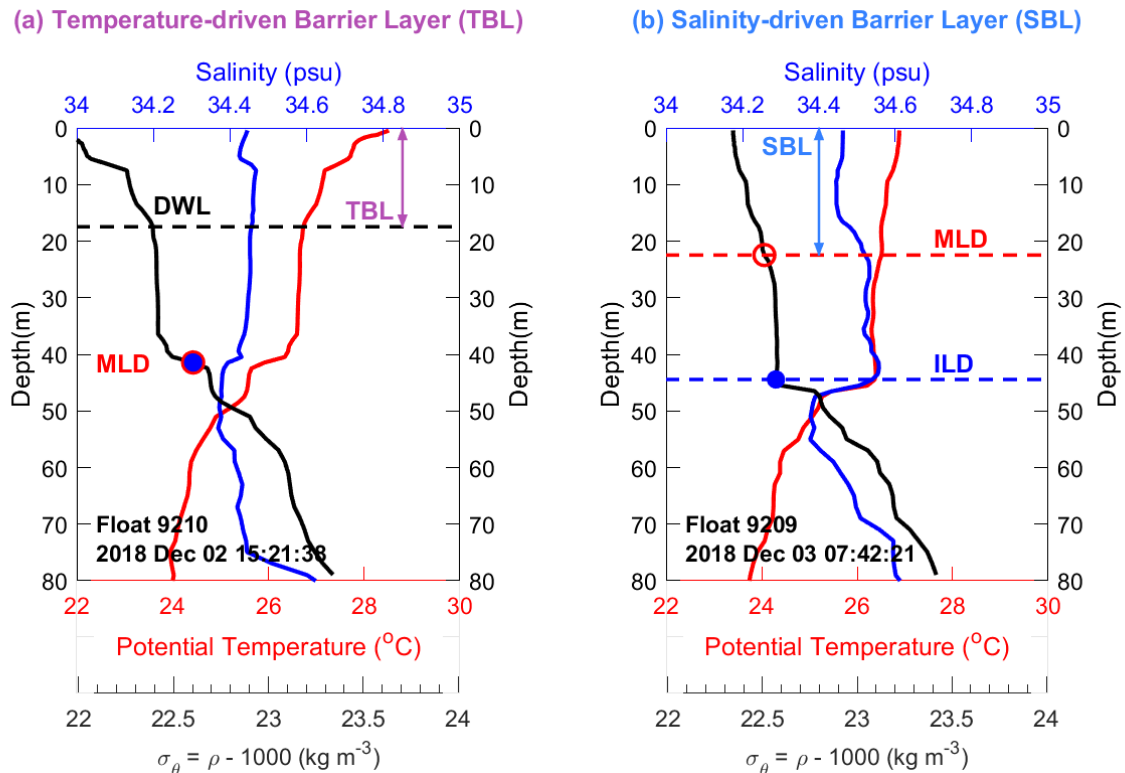
758

759 Fig. 3. Measurements of temperature (a-d) and salinity (e-h) in the upper 100 m taken by four
 760 ALAMO floats (9205, 9209, 9207 and 9210). The period of strong DV SST and MJO events are
 761 described in Feng et al. (2020). Blue lines are the estimated MLD (section 3).

762

763

764



766

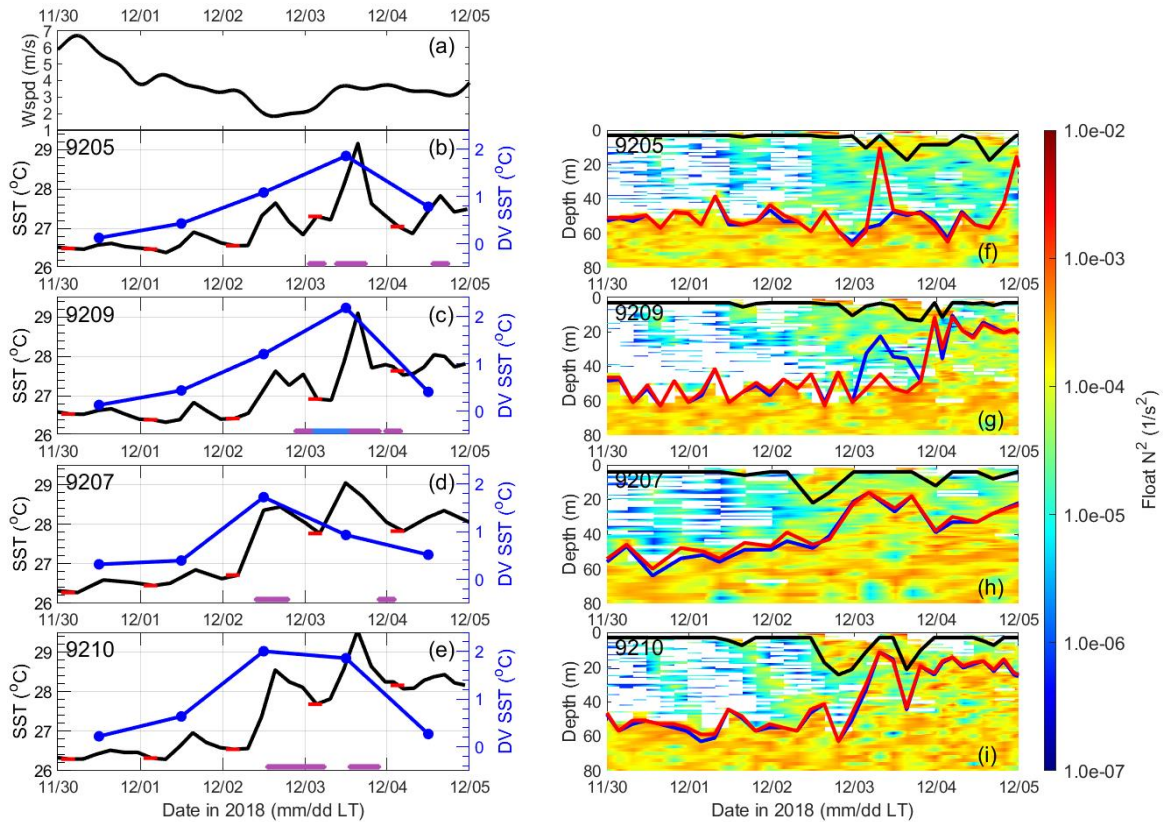
767 Fig. 4. Examples of temperature-driven barrier layer TBL (depth range indicated by the purple
 768 double arrow in a) and salinity-driven barrier layer SBL (depth range indicated by the light blue
 769 double arrow in b) based on the profiles of potential density anomaly σ_θ ($= \rho - 1000$; black lines),
 770 potential temperature (blue lines) and salinity (red lines) at floats 9210 and 9209. The surface
 771 mixed layer depth MLD (red circles and red dashed line), isothermal layer depth ILD (blue dots
 772 and blue dashed line) and diurnal warm layer depth DWL (black dashed line) are estimated. The
 773 TBL is identified if $DWL > 10$ m. The SBL is identified if $ILD - MLD > 10$ m. More

774 discussions on the criteria for identifying TBL and SBL can be found in supporting information

775 A.

776

777

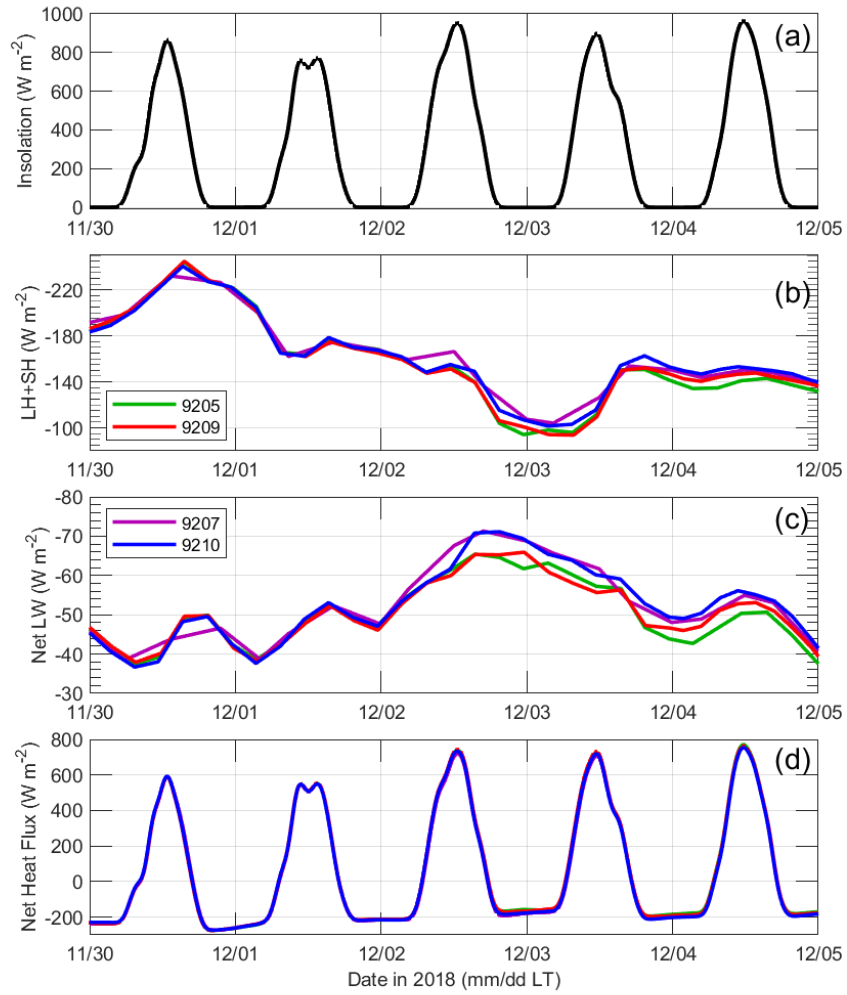


779

780 Fig. 5. Wind speed measurements on the buoy (a), and measurements of SST (black lines in b-e;
 781 referenced to the left axis), DV SST (blue dots connected with lines in b-e; referenced to the
 782 right axis) and N^2 (f-i; $N^2 < 0$ is shaded in white color) on four ALAMO floats (9205, 9207, 9209
 783 and 9210). In (b)-(e), the red lines mark the foundation SST (SST_{fund} ; referenced to the left axis)
 784 in each day, and the purple and light blue bars in (b)-(e) mark the period where TBL and SBL
 785 exist, respectively. The TBL and SBL are identified using the estimates of DWL (black lines),
 786 MLD (blue lines) and ILD (red lines) in (f)-(i).

787

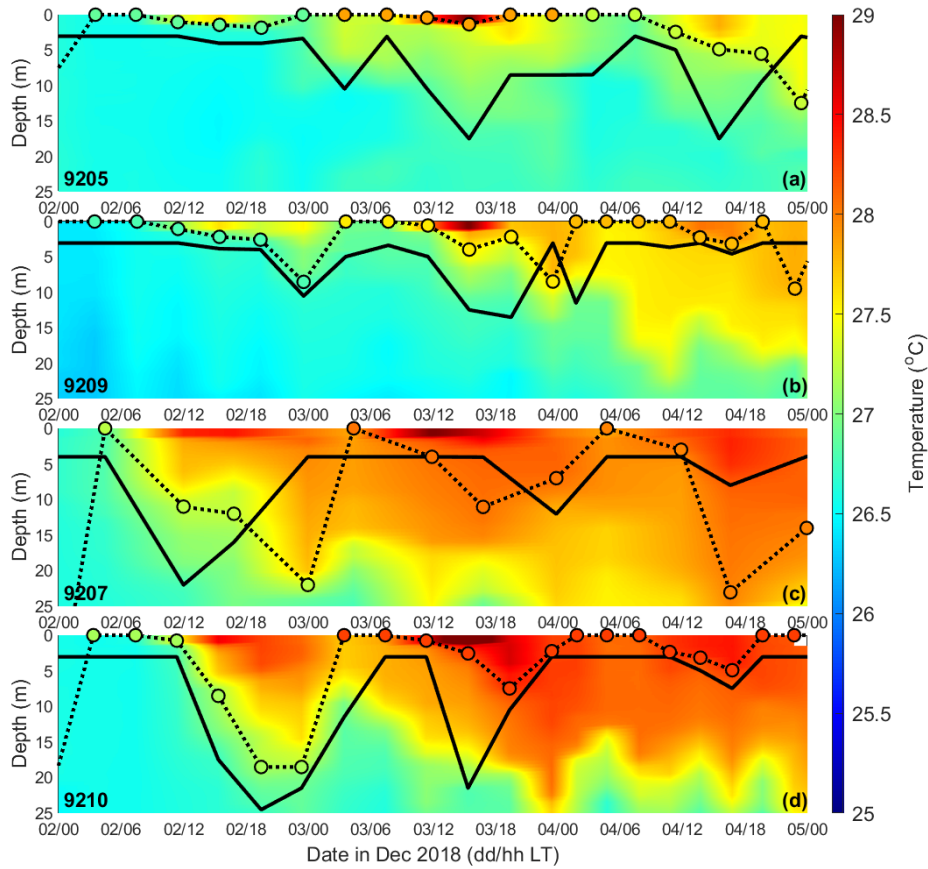
788



790
 791 Fig. 6. Measurements of insolation on the buoy (a), and estimates of latent plus sensible heat flux
 792 (b), net longwave radiation (c) and air-sea net heat flux (d) at four ALAMO floats (color lines).

793

794



795

796 Fig. 7. Measurements of temperature (color shading) in the upper 25 m, estimated DWL (black

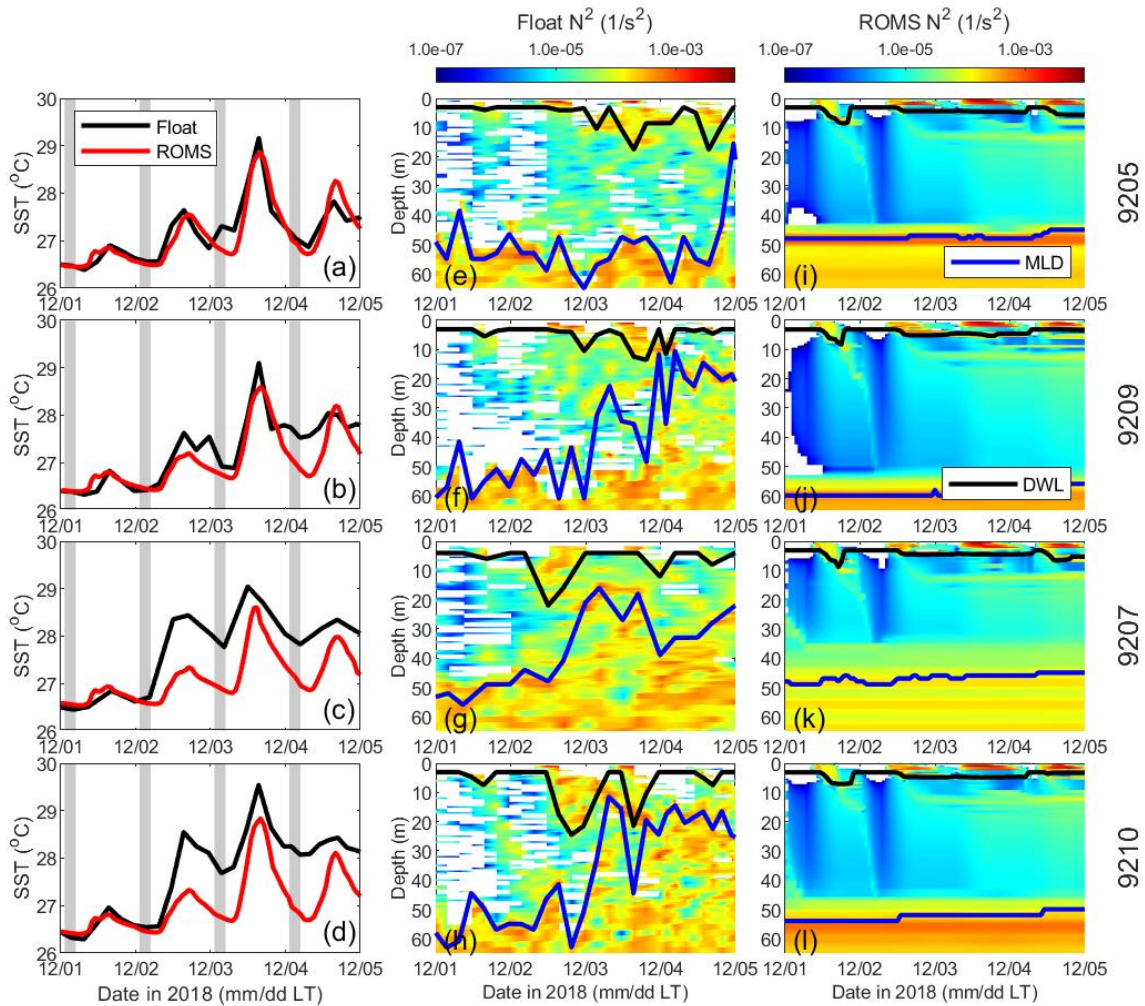
797 lines) and estimated DWL* (black dashed line connected with color dots) from Dec 2nd to 4th

798 2018 at four ALAMO floats (a-d). The color dots are the temperature T^* of the isotherm, used for

799 finding the DWL*.

800

801

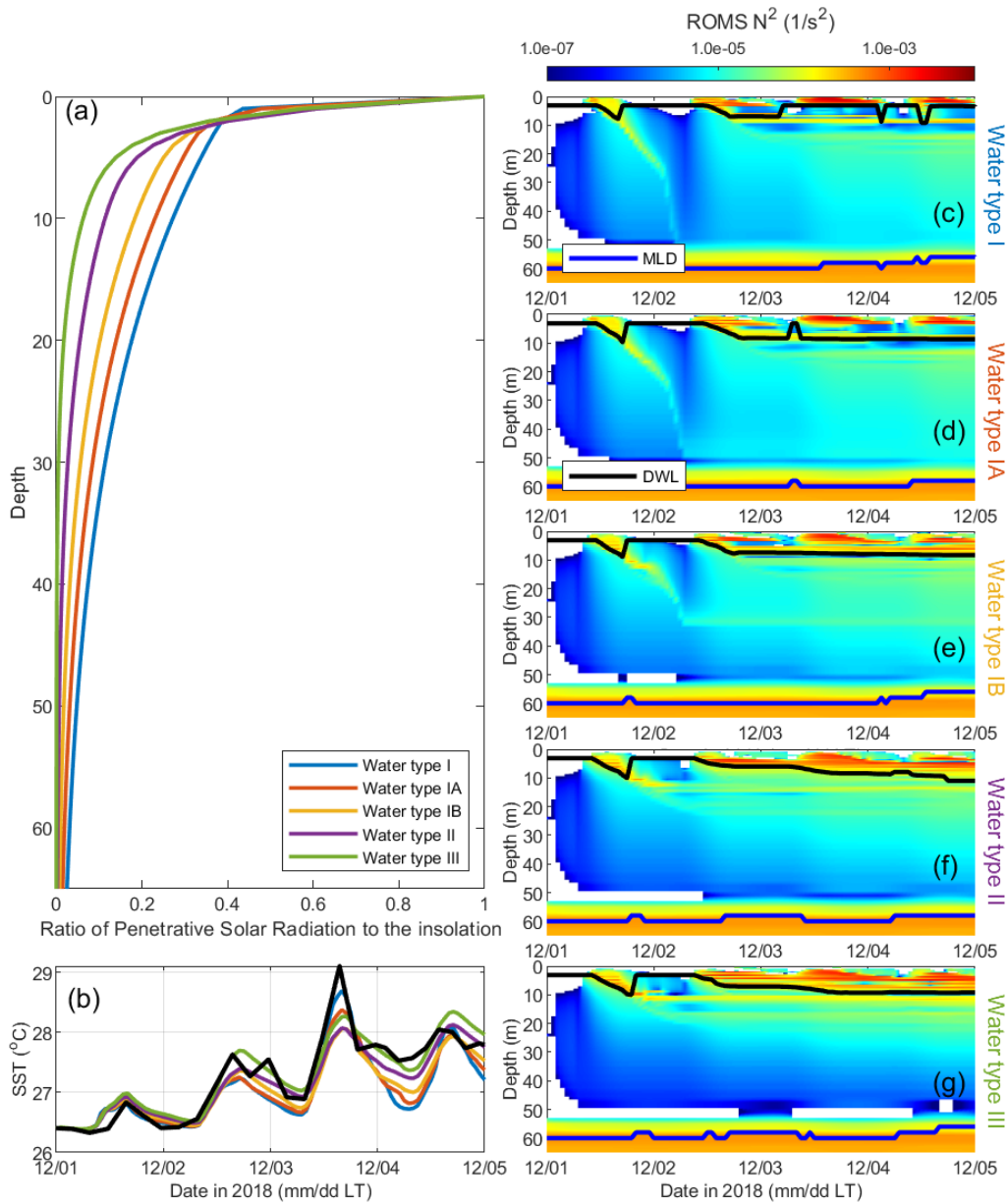


802

803 Fig. 8. Simulations of SST (red lines in a-d) and N^2 (color shading in i-l) using the KPP in the
 804 ROMS, compared with the observations of SST (black lines in a-d) and N^2 (color shading in e-h)
 805 at all ALAMO floats (each row). The period for computing the SST_{fnd} in each day is marked by
 806 the grey area in (a)-(d). The DWL (black lines) and MLD (blue lines) are estimated in (e)-(l),
 807 respectively.

808

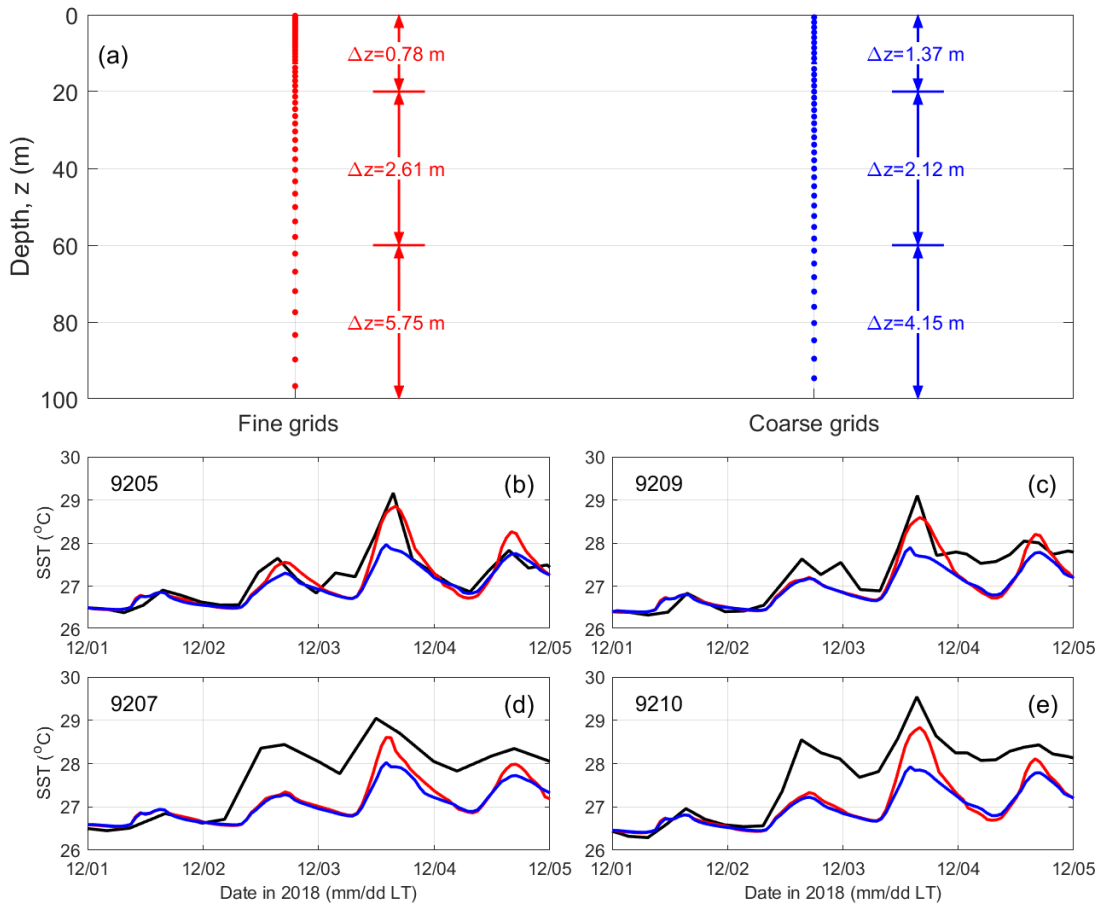
809



810

811 Fig. 9. Model results of N^2 (color shading in c-g) and SST (b) at float 9209 by varying the
 812 penetrative solar radiation based on five water types (colored lines in a and b). The DWL (black
 813 lines) and MLD (blue lines) are estimated in (c)-(g), respectively. The ratio of penetrative solar

814 radiation to the insolation at different depth during the model simulations is shown in (a). The
815 black line in (b) is the float-measured SST.



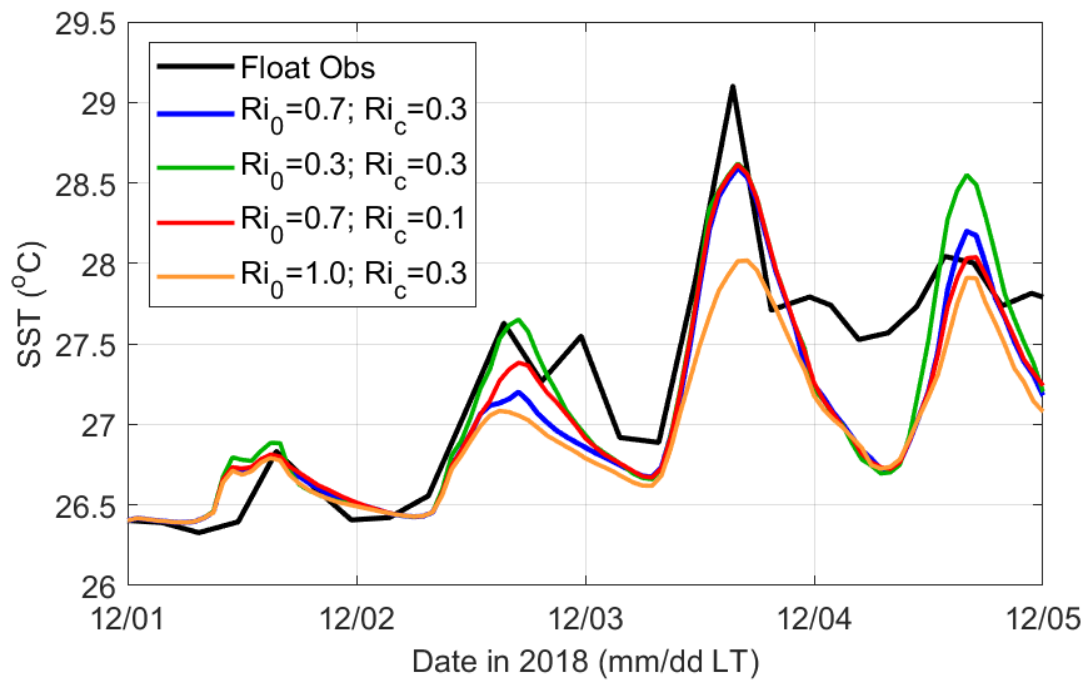
816

817 Fig. 10. Model results of SST at four ALAMO floats (b-e) simulated using two types of vertical
 818 grids (a) in the KPP: fine (red lines) and coarse grids (blue lines), with the comparison to the
 819 float measurements (black lines), where Δz in (a) is the average of vertical resolution in different
 820 range of depth.

821

822

823



824

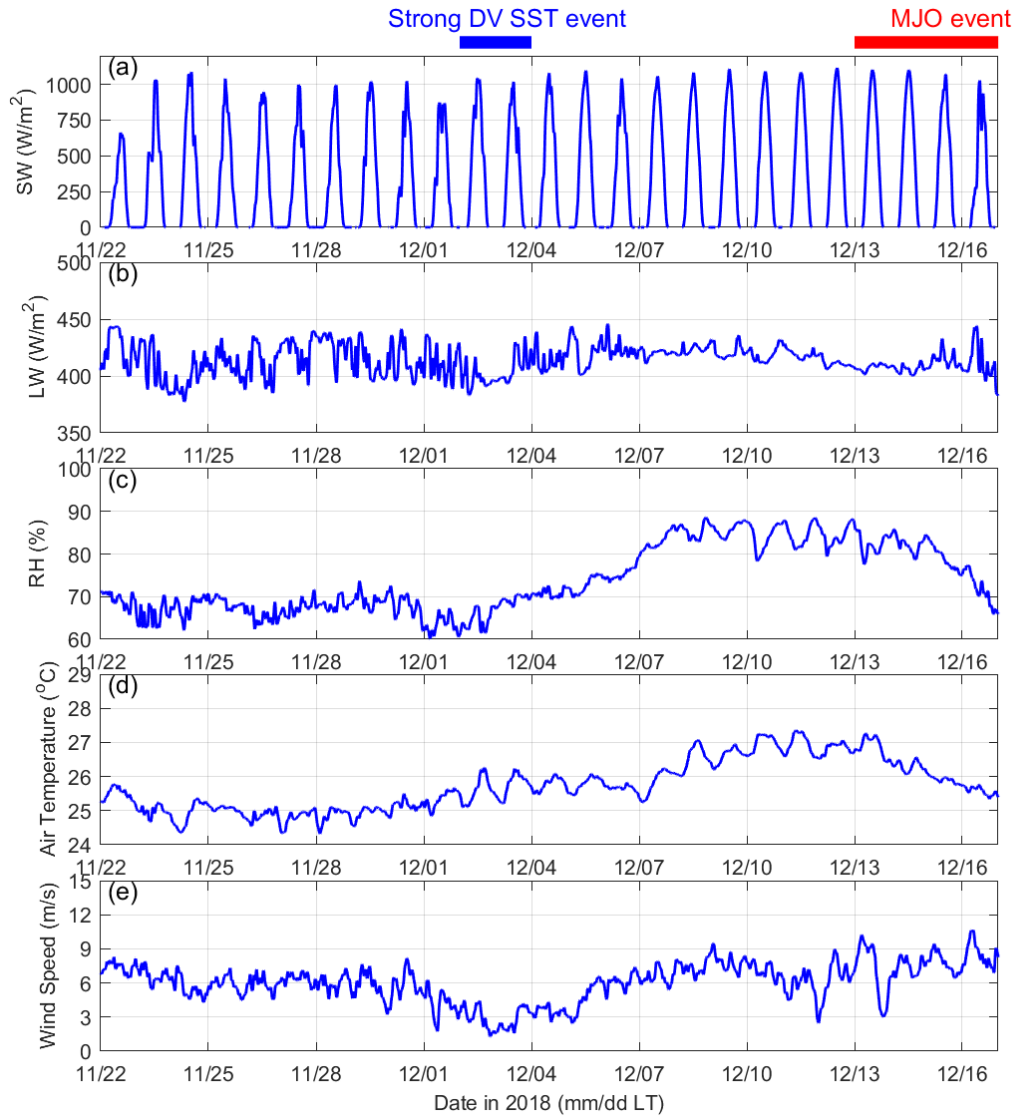
825

826 Fig. 11. Simulations of SST at float 9209 by different set of the mixing parameters Ri_0 and Ri_c

827 (blue: $Ri_0 = 0.7$ and $Ri_c = 0.3$; green: $Ri_0 = 0.3$ and $Ri_c = 0.3$; red: $Ri_0 = 0.7$ and $Ri_c = 0.1$; orange:

828 $Ri_0 = 1.0$ and $Ri_c = 0.3$), with the comparison to the float observation (black).

829



830

831 Fig. 12. Measurements of downward shortwave radiation SW (a), downward longwave radiation

832 LW (b), relative humidity RH at 3-m height above the sea surface (c), air temperature at 3-m

833 height above the sea surface (d), and wind speed at 4-m height above the sea surface (e) on the

834 FIO buoy. The period of the strong DV SST and MJO events are described in Feng et al. (2020).

835

836

837

Figure1.

Figure2.

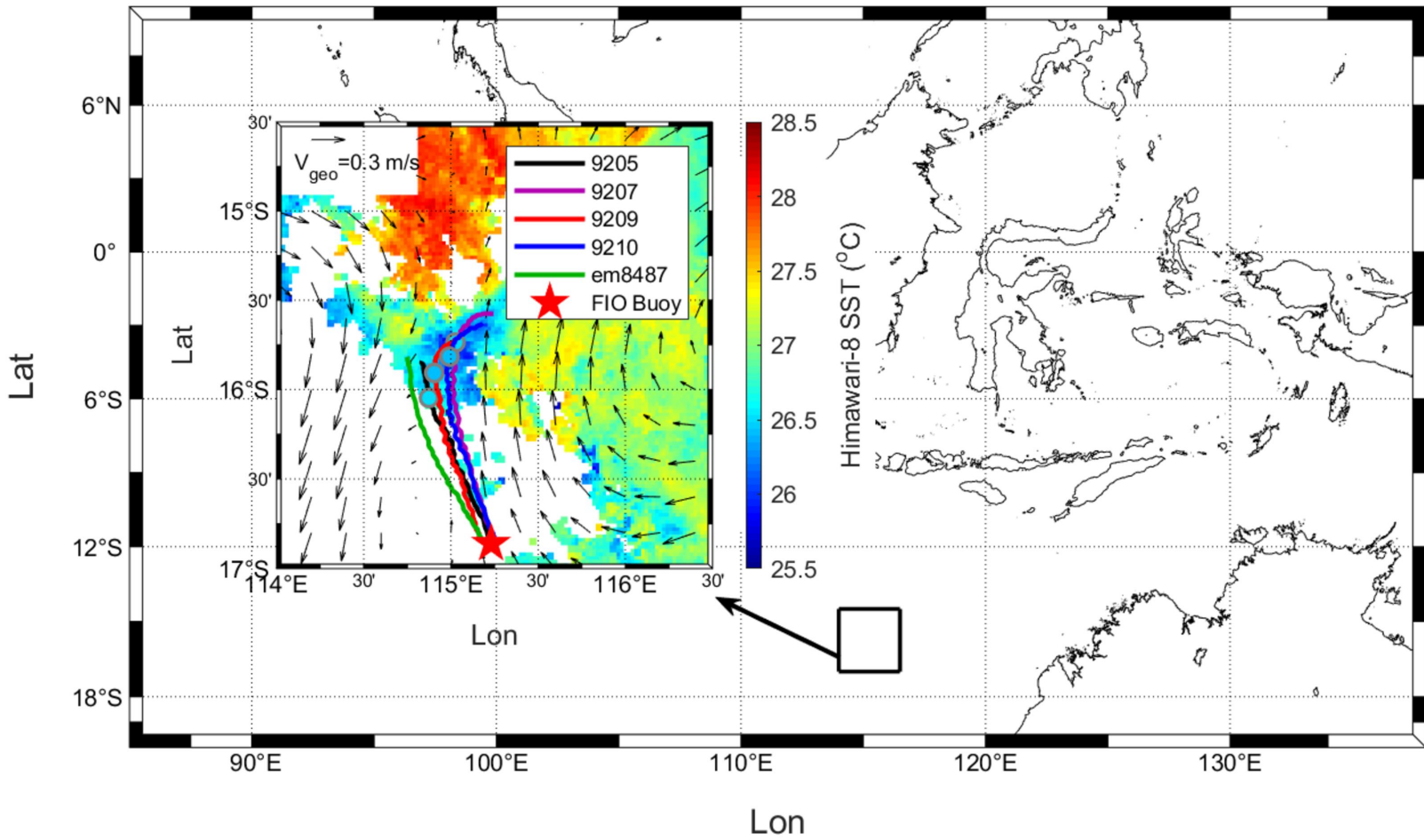
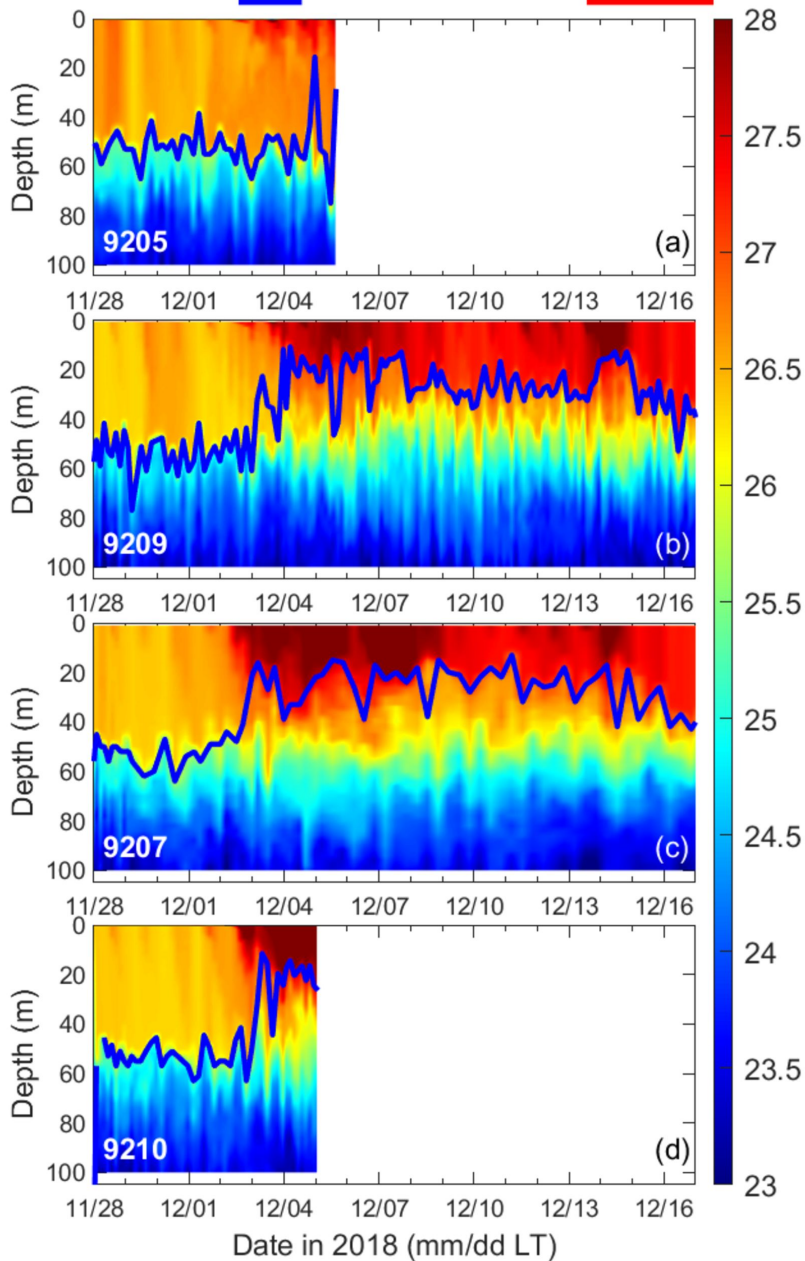


Figure3.

Strong DV SST event

MJO event



Strong DV SST event

MJO event

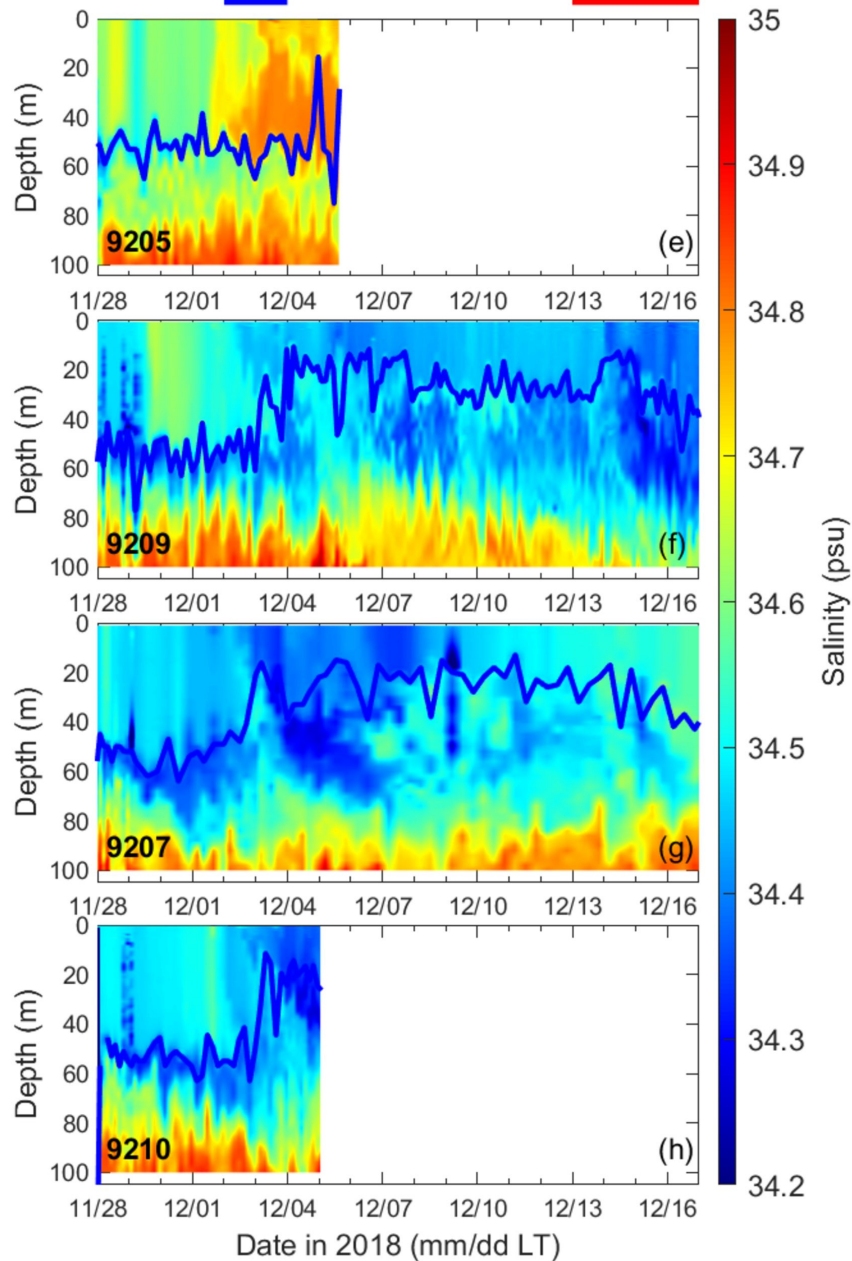
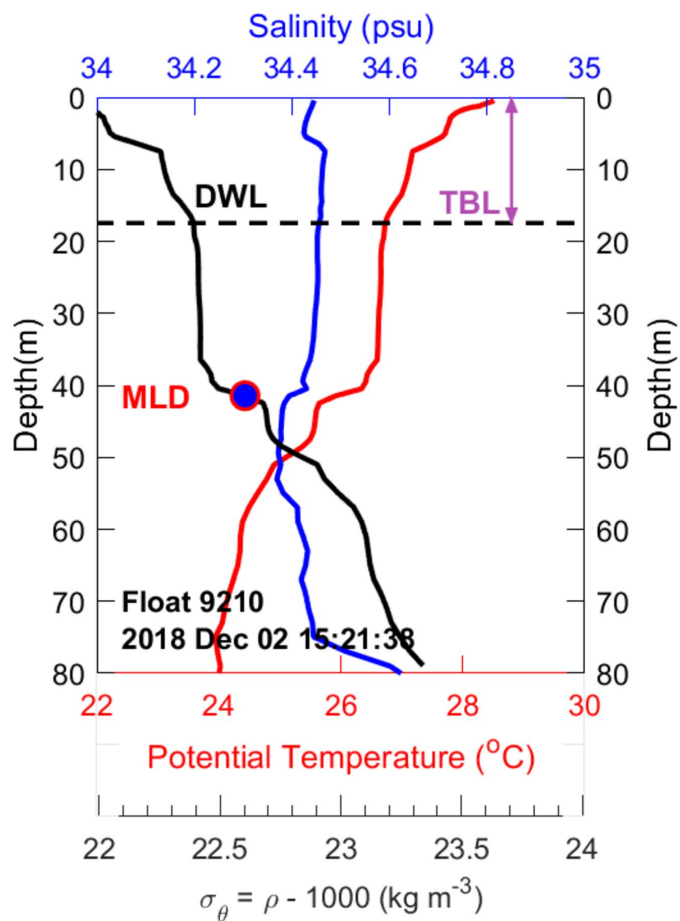


Figure4.

(a) Temperature-driven Barrier Layer (TBL)



(b) Salinity-driven Barrier Layer (SBL)

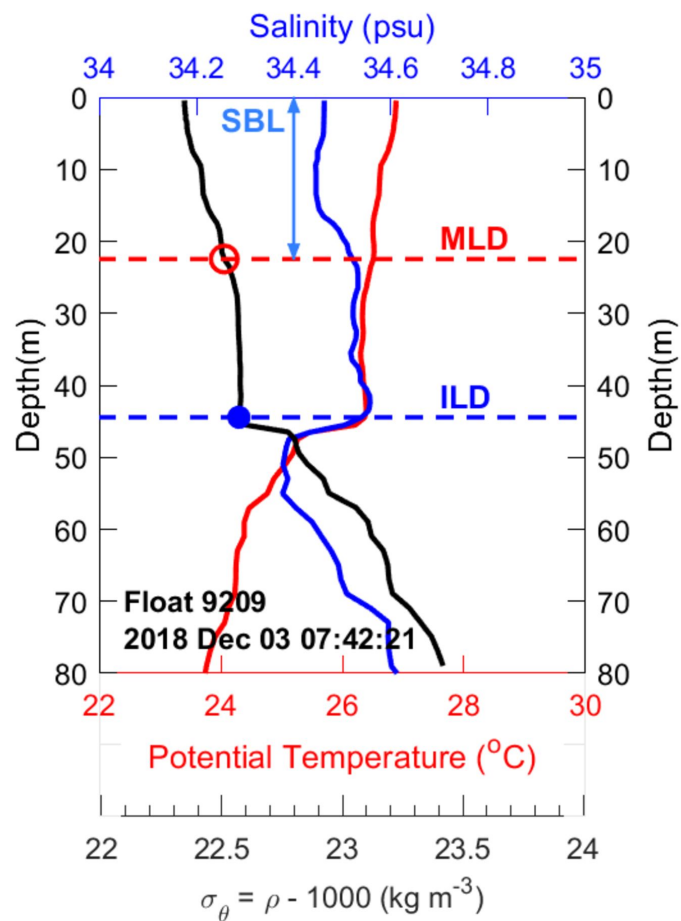


Figure5.

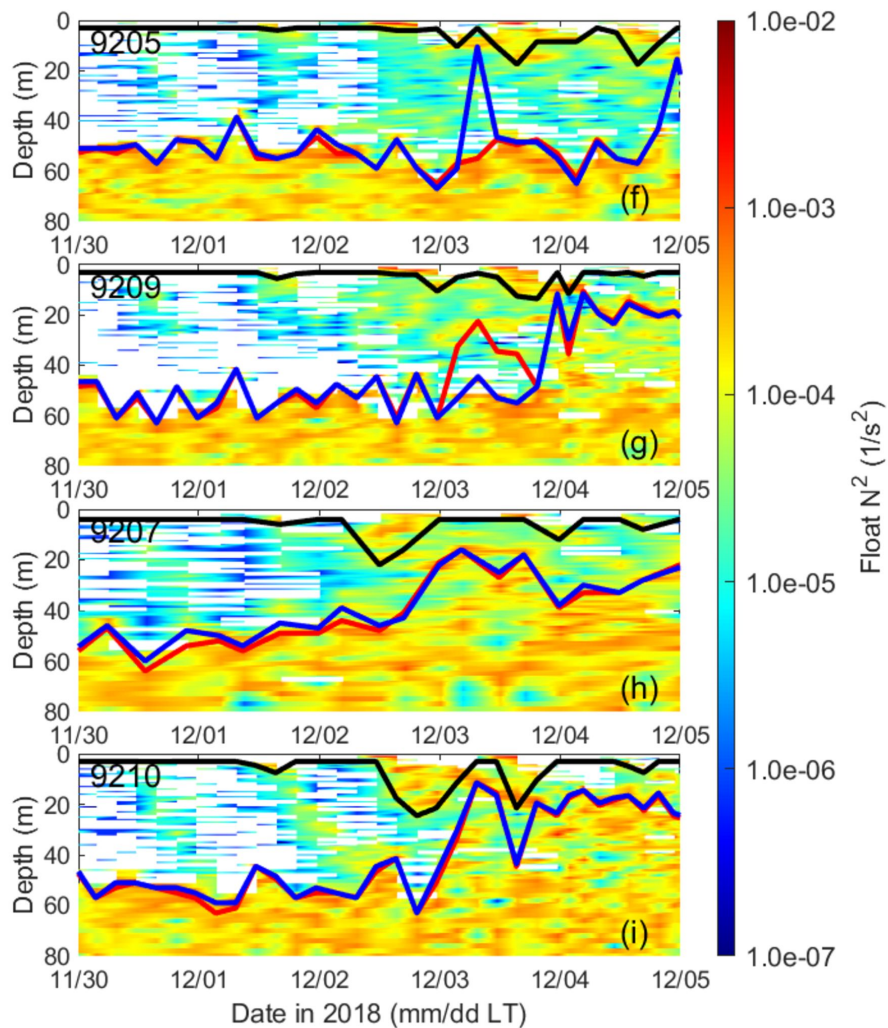
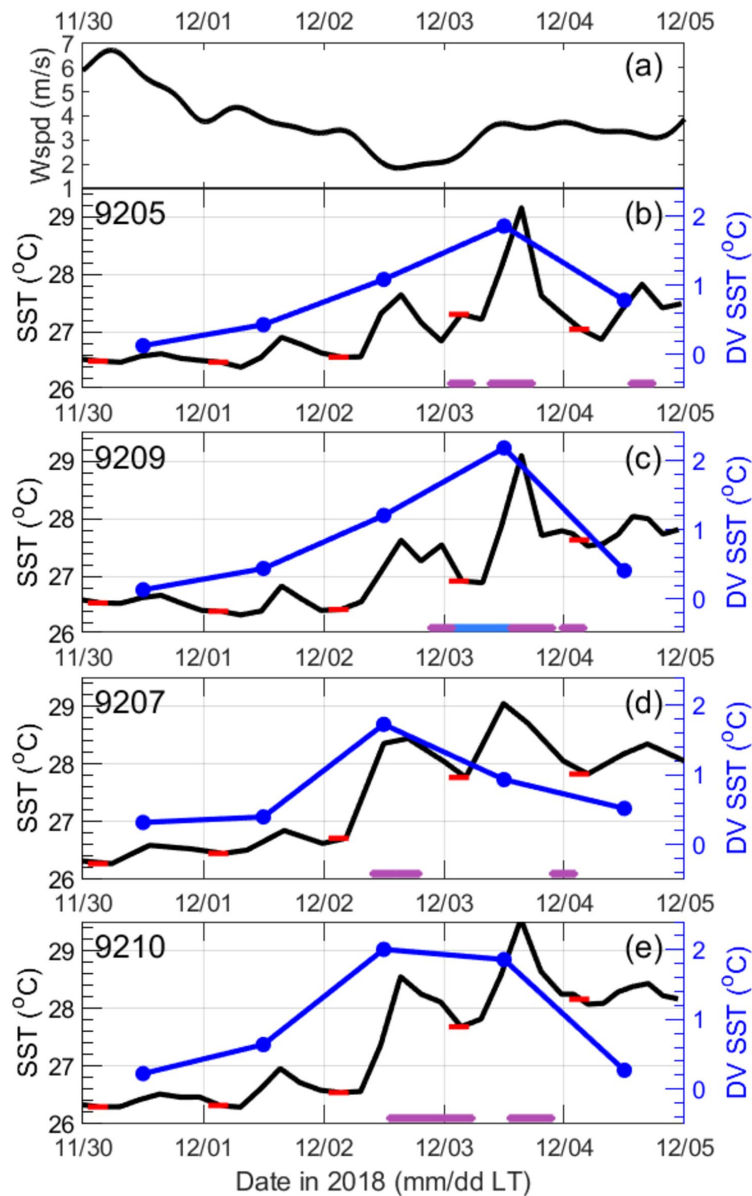
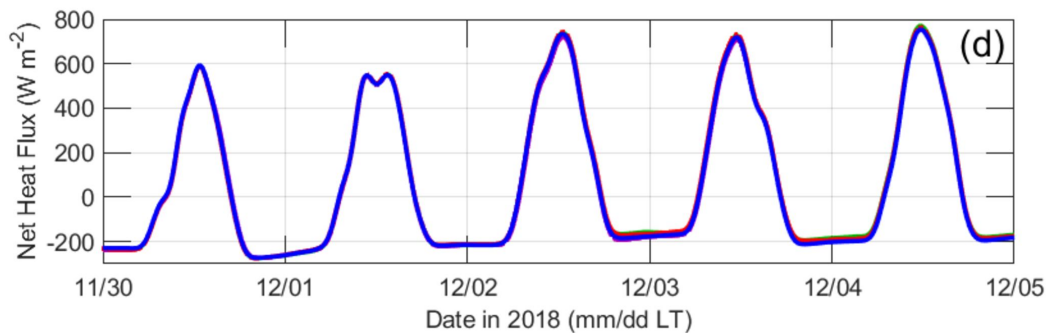
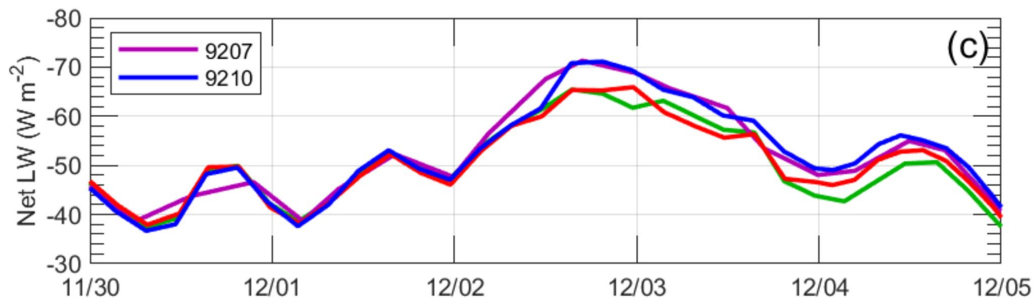
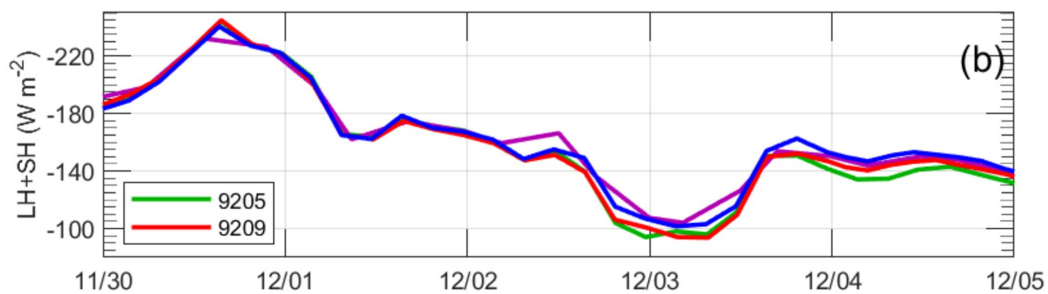
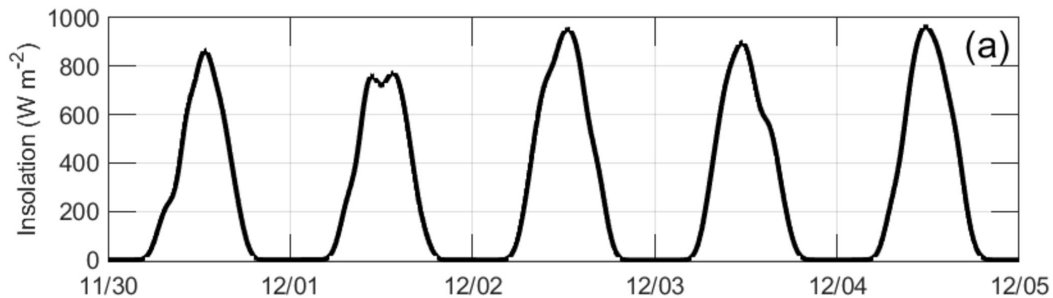


Figure6.



Date in 2018 (mm/dd LT)

Figure7.

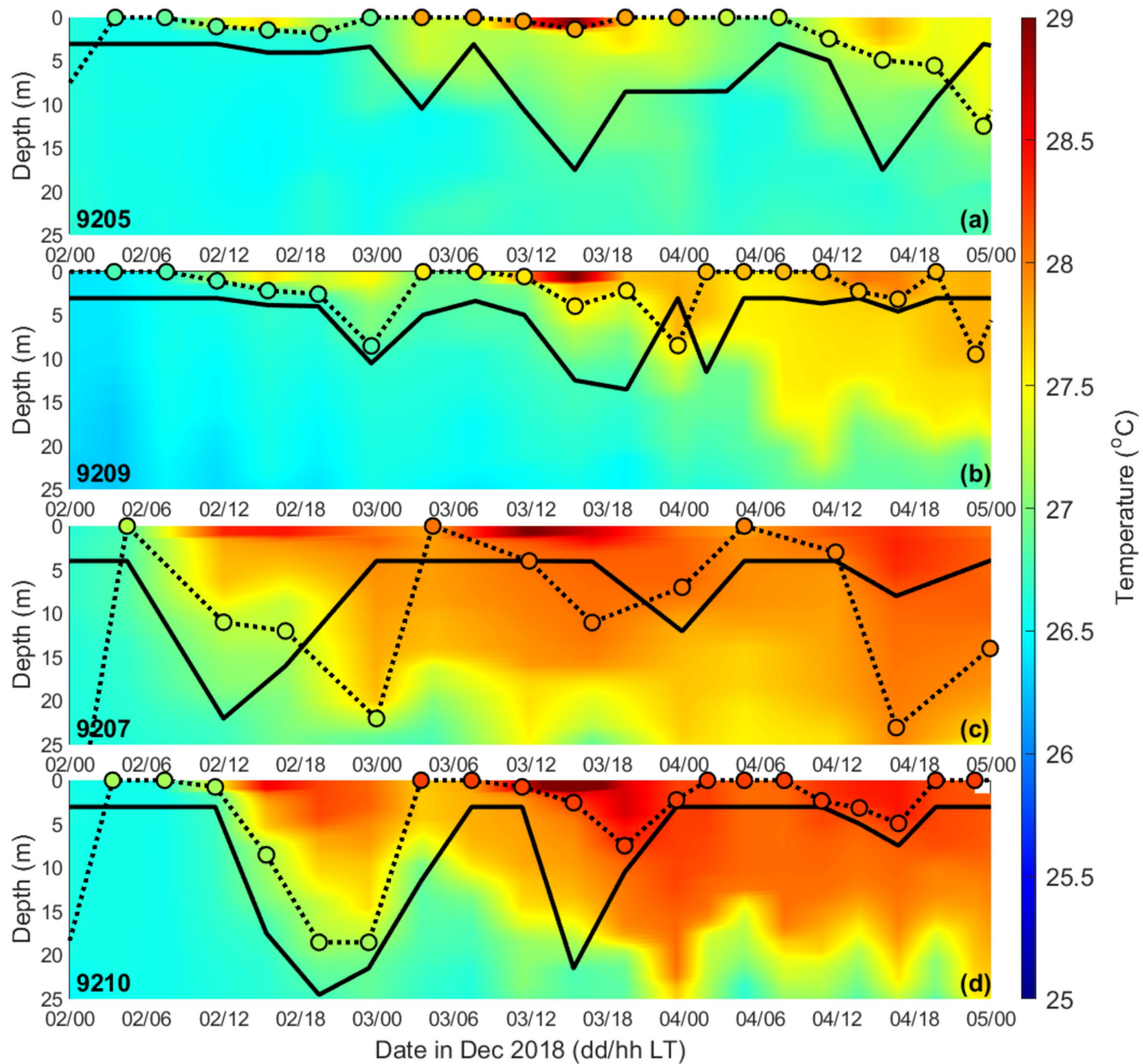


Figure 8.

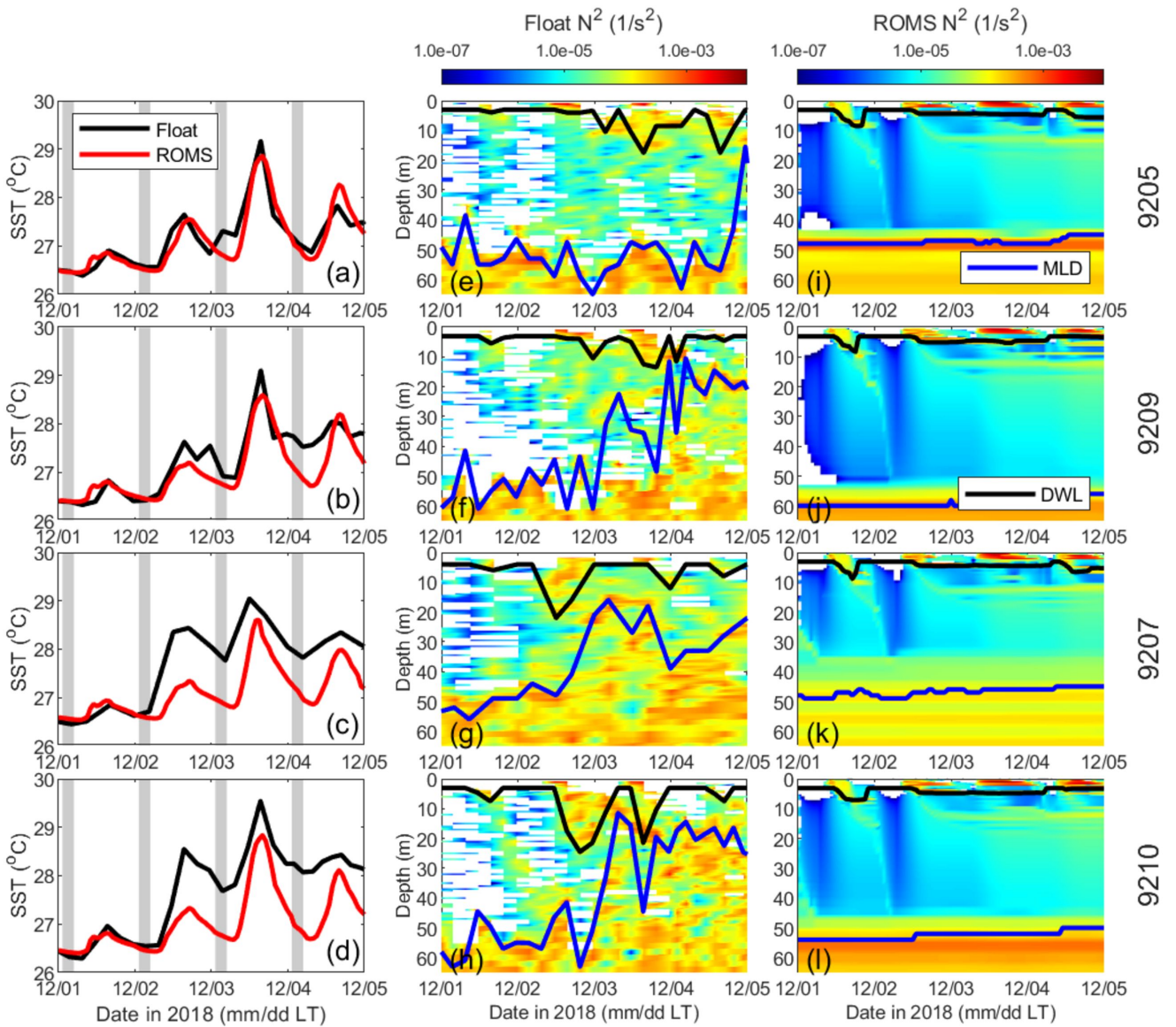


Figure9.

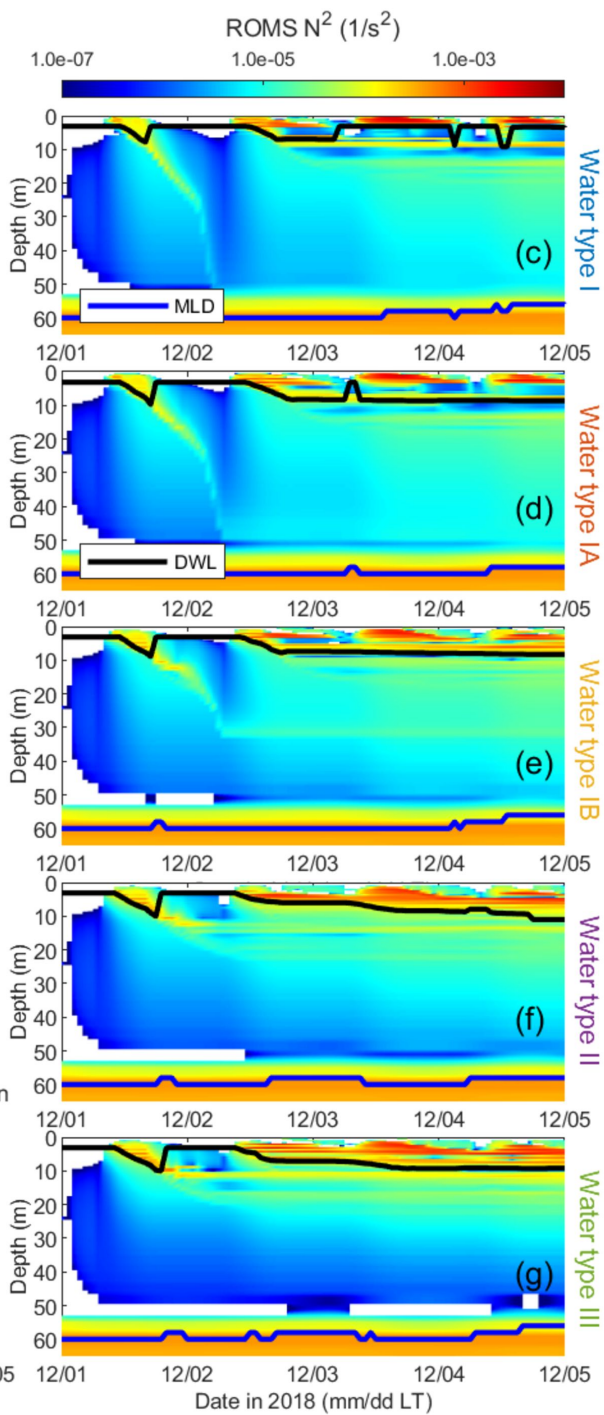
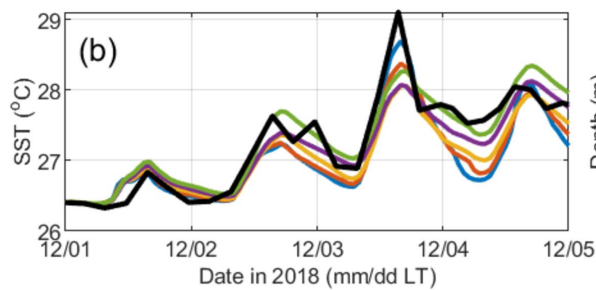
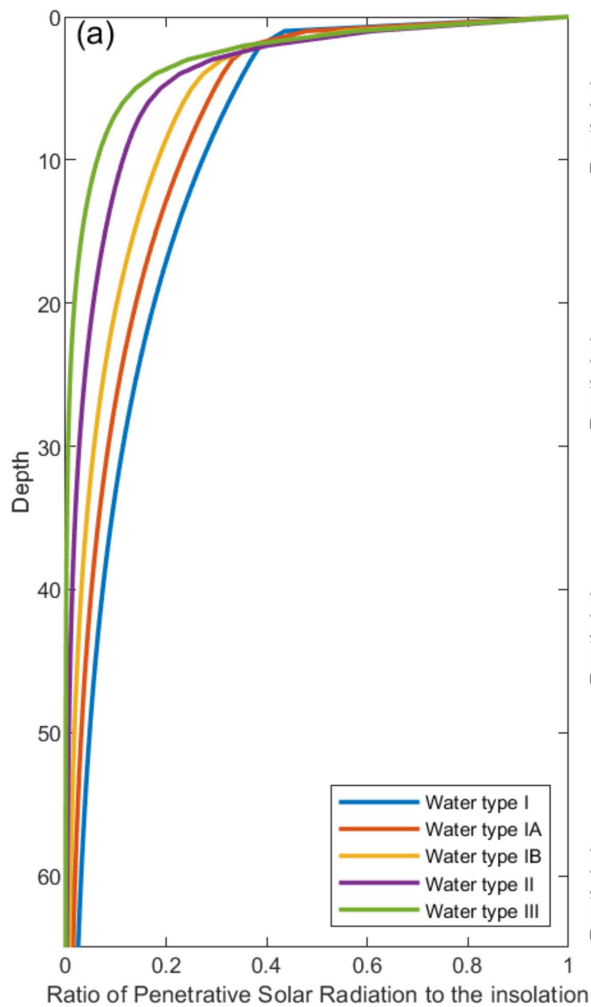


Figure10.

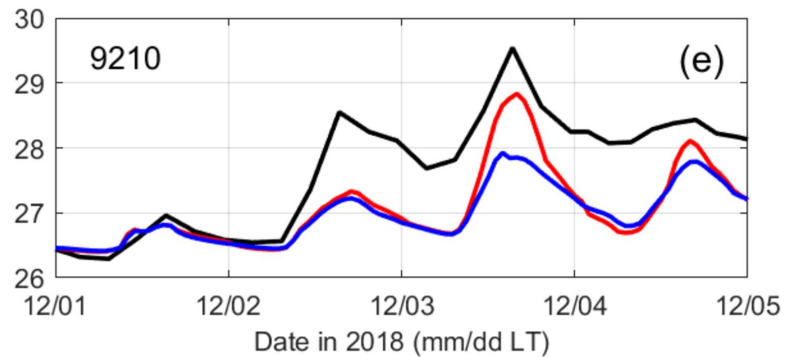
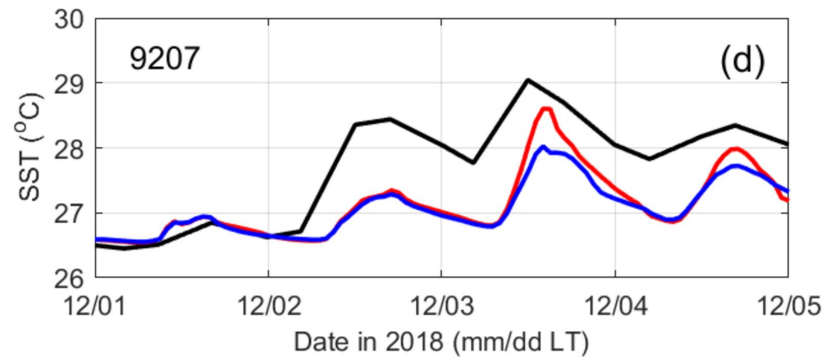
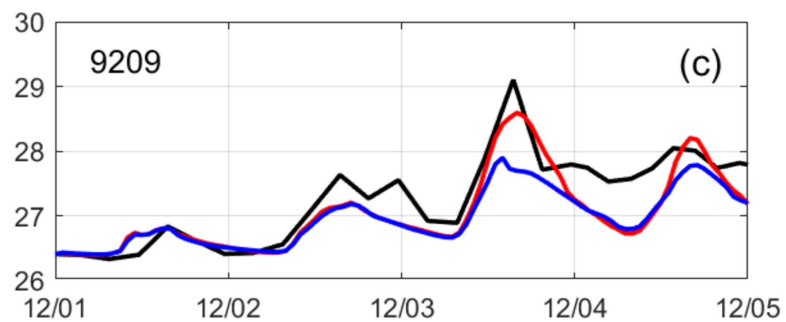
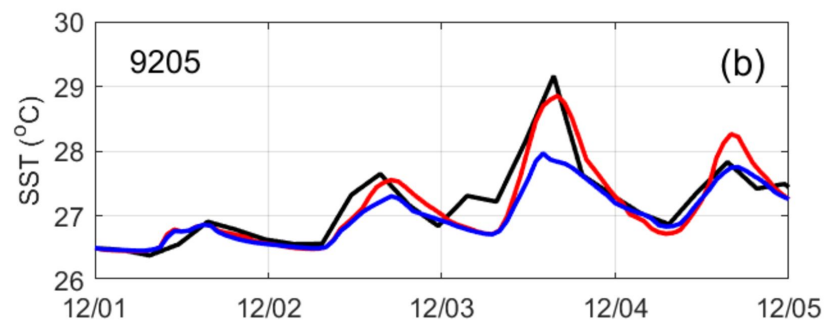
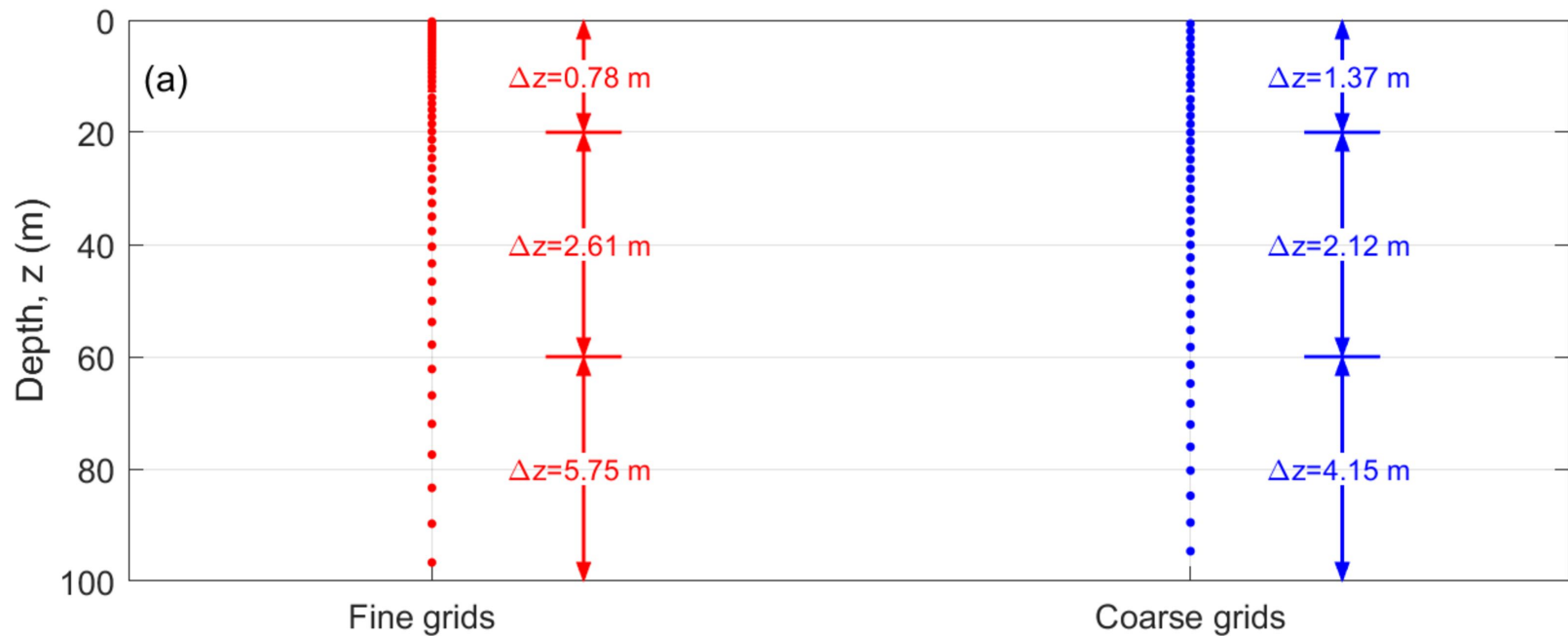


Figure11.

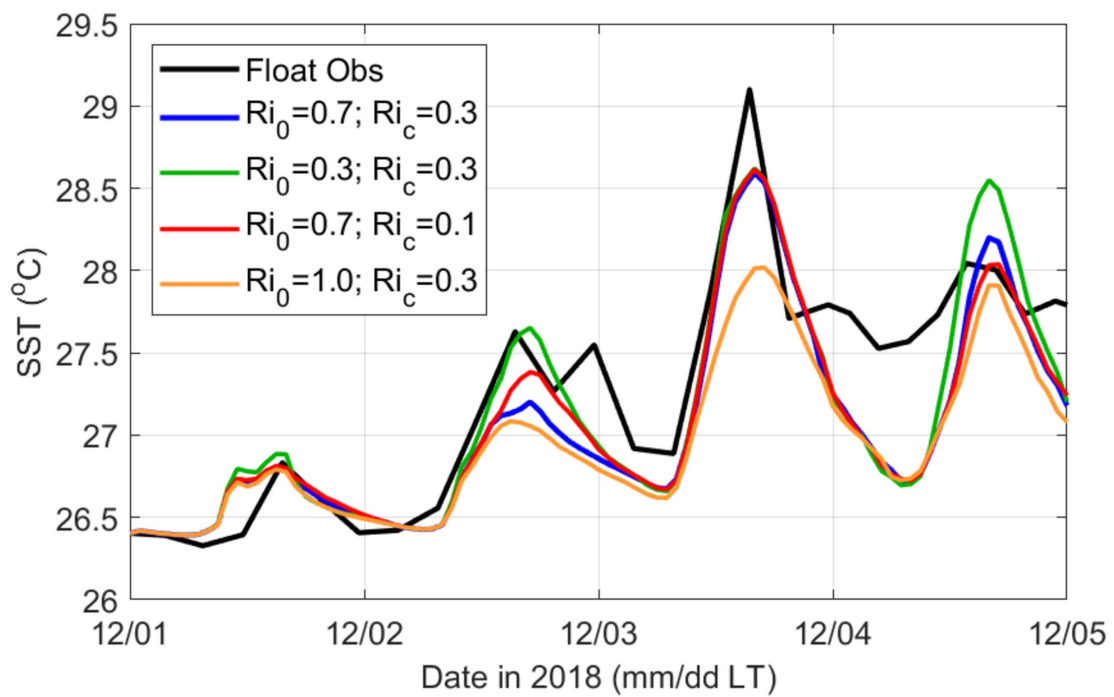


Figure12.

Strong DV SST event

MJO event

